

NeuroPMD: Neural Fields for Density Estimation on Product Manifolds

William Consagra

Department of Statistics, University of South Carolina

Zhiling Gu

Department of Biostatistics, Yale University

Zhengwu Zhang

Department of Statistics and Operations Research, University of North Carolina at Chapel Hill

January 7, 2025

Abstract

We propose a novel deep neural network methodology for density estimation on product Riemannian manifold domains. In our approach, the network directly parameterizes the unknown density function and is trained using a penalized maximum likelihood framework, with a penalty term formed using manifold differential operators. The network architecture and estimation algorithm are carefully designed to handle the challenges of high-dimensional product manifold domains, effectively mitigating the curse of dimensionality that limits traditional kernel and basis expansion estimators, as well as overcoming the convergence issues encountered by non-specialized neural network methods. Extensive simulations and a real-world application to brain structural connectivity data highlight the clear advantages of our method over the competing alternatives.

Keywords: Deep Neural Network, Density Estimation, Functional Data Analysis, Manifold Domain, Neural Field

1 Introduction

This work considers the problem of density (and intensity) estimation on the D -product manifold, denoted $\Omega := \times_{d=1}^D \mathcal{M}_d$, where each marginal domain \mathcal{M}_d is a closed Riemannian manifold of dimension $p_d \geq 1$. Our particular focus is on the big data (large sample size n) and high-dimensional ($D \geq 2$) setting.

Product manifold-based point set data arise in a wide range of fields, including neuroscience (Moyer et al., 2017), genomics/proteomics (Pavlos Zoubouloglou and Marron, 2023), and climate science (Begu et al., 2024). Our work is specifically motivated by an application in the emerging field of *structural connectomics*, a subfield of neuroscience that studies the physical pattern of neural connections formed by white matter fibers across the cerebral cortex (Chung et al., 2021). These connections can be inferred using modern high-resolution neuroimaging techniques, which map the endpoints of the fibers directly onto the cortical surface (St-Onge et al., 2018) (see Figure 1 panel A). The resulting endpoint connectivity data can be considered a point set on $\Omega = \times_{d=1}^2 \mathcal{M}_d$, where $\mathcal{M}_d \subset \mathbb{R}^3$ denotes the cortical surfaces. These connections are visualized as paired red and blue points in Figure 1 panel B. The goal is to estimate the density function of the connectivity on Ω , which is commonly referred to as the continuous structural connectivity in the literature (Moyer et al., 2017; Consagra et al., 2024a). However, this high-dimensional, big data setting, with $D = 2, p_1 = p_2 = 2$, and $n > 10^6$, poses significant computational and statistical challenges for classical density estimators. Consequently, many existing connectivity analysis methods coarsen the connectivity data using a low-resolution brain atlas, masking high-resolution connectivity information that could offer critical insights into key neuroscience questions.

1.1 Related Work

A substantial body of work exists for nonparametric kernel density estimation (KDE) on Riemannian manifolds (Pelletier, 2005; Kim and Park, 2013; Bates and Mio, 2014; Berry and Sauer, 2017; Cleanthous et al., 2020; Ward et al., 2023). These methods can naturally be extended to the product space Ω by forming a D -product of the marginal kernels. However, KDE becomes computational problematic for large n and D , as naive point-wise estimation requires at least $O(n \sum_{d=1}^D p_d)$ operations. Computation is further complicated on the

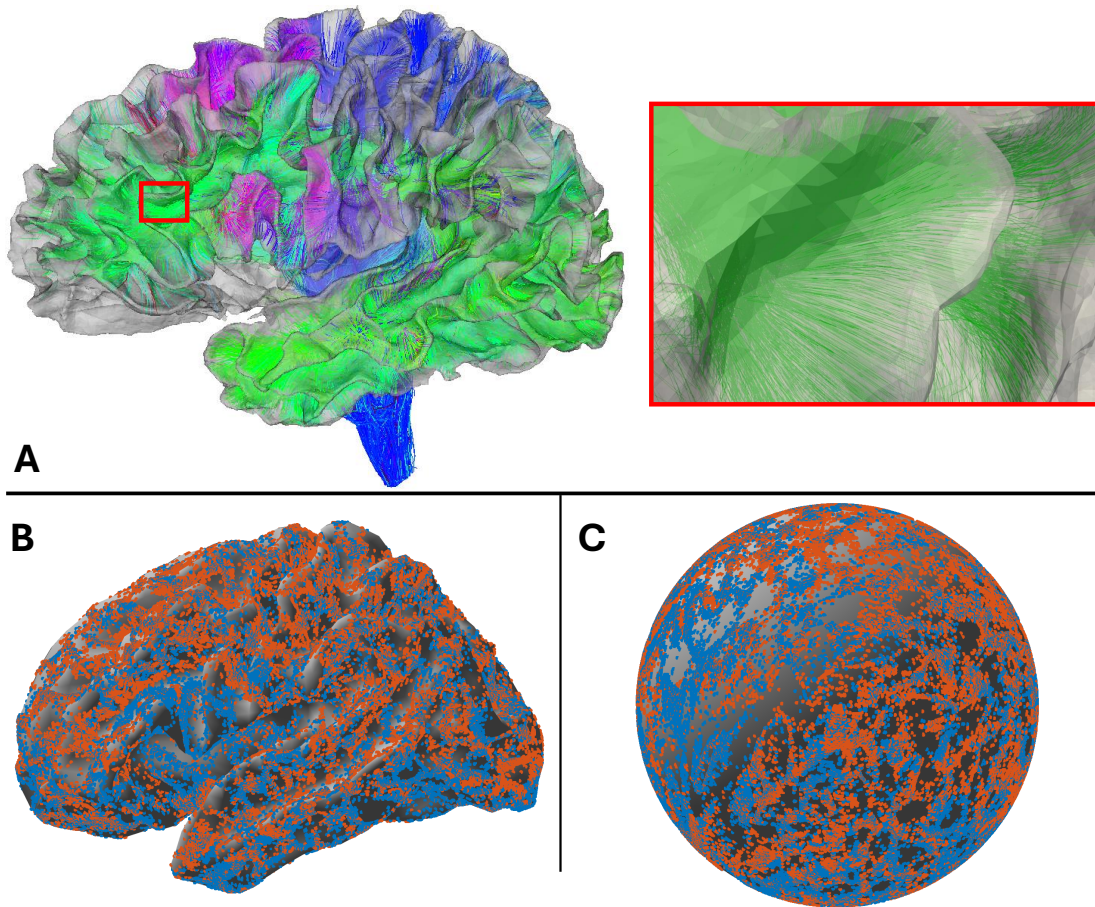


Figure 1: Product manifold point process data from a neuroscience connectomics application. A) Cortical surface mesh of the left hemisphere with representative white matter fiber connections. The red zoomed-in region highlights fibers terminating on the surface. B) Observed endpoints on the surface. Each red point corresponds with a single blue point, which together form the surface coordinates of a connection. C) Observed endpoints represented under spherical parameterization.

manifold domain, as many methods require repeated calculation of geodesic distances or exponential/log map, which can incur additional computational overhead. While approximation techniques for accelerating computation exist for Euclidean spaces (Bentley, 1975; Karppa et al., 2022), adapting these methods to high-dimensional manifold domains is complicated and cumbersome. Additionally, bandwidth selection for KDE-based methods is notoriously challenging for high-dimensional domains, often resulting in locally excessive and/or insufficient smoothing due to the varying smoothness of the underlying function across the domain (Wang and Scott, 2019).

An alternative line of research models the density (or intensity) function using para-

metric approaches based on linear basis expansion (Simpson et al., 2016; Ferraccioli et al., 2021; Arnone et al., 2022; Begu et al., 2024). These methods alleviate the computational burden of the non-parametric approaches in large n settings, as computational costs generally scale with the number of basis functions rather than the number of observations. Additionally, many basis systems serve as universal approximators, capable of representing most functions of interest by selecting a sufficiently large rank. However, these methods are typically limited to relatively low-dimensional domains due to the computational curse of dimensionality, as the parameter space often grows exponentially with D to maintain approximation accuracy. Data-driven approaches have been proposed to construct more parameter-efficient functional basis for representation (Chen and Jiang, 2017; Wang et al., 2020; Wang and Cao, 2022; Consagra et al., 2024b). However, these methods often rely on the availability of replicated functions and assume a direct observation model (signal plus noise framework), neither of which hold in our setting.

Recent developments in the machine learning community have introduced flexible density/intensity estimators based on neural networks (Xiao et al., 2017; Mei and Eisner, 2017; Zhou and Yu, 2023), though these approaches primarily focus on the Euclidean setting (temporal and spatiotemporal domains). A notable exception is the work by Tsuchida et al. (2024), who extended the squared neural density estimation framework of (Tsuchida et al., 2023) to some simple product manifolds. However, their method relies on custom-designed activation functions that facilitate a closed-form expression of the normalization integral under the Poisson process likelihood, which limits flexibility. Moreover, their network estimator is shallow, consisting of only two layers, and deep extensions are non-trivial due to the aforementioned closed-form integrability requirement. Although deep networks are not strictly necessary for universal approximation in the infinite-width limit (Hornik et al., 1989), empirical (Krizhevsky et al., 2012) and theoretical (Telgarsky, 2015; Eldan and Shamir, 2016) findings suggest that deep architectures can be significantly more parameter-efficient than wider ones. Thus, the restriction to shallow architectures is a major limitation, as deep networks typically require far fewer parameters to approximate functions of equivalent complexity.

1.2 Our Contribution

In this work, we develop a general deep neural network-based density estimator for product Riemannian manifolds. By leveraging the parameter efficiency of deep, fully connected neural networks, our approach avoids the computational curse of dimensionality that plagues classical basis function estimators. Once trained, point-wise inference requires only a forward pass through the network, which can be efficiently executed on a GPU, offering significant improvements in computational scalability compared to KDE.

While the parameter efficiency and inference speed of deep neural network based function representations are highly desirable in our setting, their estimation is complicated by the so-called *spectral bias*, the tendency of the network to learn overly smooth function approximations and exhibit slow convergence to high frequency components (Rahaman et al., 2019). While this phenomenon has been linked to strong generalization properties in certain tasks (Cao et al., 2019), it is typically undesirable when using neural networks to parameterize continuous functions, as it can make learning important high-frequency functional features difficult. To combat this issue, we propose a first-layer basis expansion inspired by Fourier features (Rahimi and Recht, 2007; Tancik et al., 2020). Specifically, our approach constructs these basis functions, termed *encoding functions*, by sampling random subsets from the full tensor product set of marginal Laplace-Beltrami eigenfunctions. This design enables the efficient modeling of rich, high-frequency functional features while simultaneously avoiding exponential parameter growth that would result from using a complete tensor product basis, i.e., the computational curse of dimensionality. We demonstrate this property empirically and, for the special case of the D -dimensional torus, theoretically, showing that our approach generates a representation space where elements are linear combinations of a large set of sinusoidal basis functions whose number grows rapidly with network depth, underscoring the expressive power provided by layer composition in deep networks.

Our estimation framework employs a penalized maximum likelihood objective optimized via a custom stochastic gradient ascent based algorithm. Explicit computation of high-dimensional integrals in the objective function is avoided by forming unbiased estimates of their gradients via Monte-Carlo approximations, thereby avoiding any re-introduction

of the curse of dimensionality during network training. To control the smoothness of the estimator, we incorporate a penalty term derived from the Laplace-Beltrami operator, offering computational forms in both intrinsic and extrinsic coordinates for convenience. We evaluate our method on both challenging simulated and real-world datasets, demonstrating clear improvements over classical approaches, including KDE and linear basis expansion, as well as baseline deep neural networks, which lack the architecture and task-specific training optimizations of our approach.

The rest of this paper is organized as follows: Section 2 provides relevant background and formalizes our estimation problem. Section 3 details the proposed network architecture and provides some theoretical analysis of its approximation power. Section 4 proposes an estimation algorithm for learning network parameters along with supporting implementation details including hyperparameter selection. Section 5 presents simulation studies and a real data application in brain structural network modeling. Concluding remarks are provided in Section 6. Proofs for all propositions and theorems can be found in Supplemental Section S1.

2 Background and Models

2.1 Geometric Preliminaries

Let (\mathcal{M}_d, g_d) be a closed p_d -dimensional Riemannian manifold with $\mathcal{M}_d \subset \mathbb{R}^{m_d}$ and induced metric g_d . We consider the product space $\Omega = \times_{d=1}^D (\mathcal{M}_d, g_d)$, formed by the Cartesian product of the manifolds \mathcal{M}_d . This space has a total dimension of $\sum_{d=1}^D p_d$ and inherits a way to measure distance and volumes from the individual metrics g_d of the constituent spaces \mathcal{M}_d via the metric $\sum_{d=1}^D g_d$. Denote $d\omega$ as the product volume form on Ω , analogous to the Lebesgue measure, constructed from the measures on the marginal manifolds \mathcal{M}_d using the metrics g_d .

Analogous to the Laplacian on \mathbb{R}^{m_d} , a smooth Riemannian manifold \mathcal{M}_d is equipped with a linear operator $\Delta_{\mathcal{M}_d} : C^\infty(\mathcal{M}_d) \mapsto C^\infty(\mathcal{M}_d)$, known as the *Laplace-Beltrami operator* (LBO), where $C^\infty(\mathcal{M}_d)$ is the space of smooth functions on \mathcal{M}_d . To define the LBO, we must consider the differential geometry of \mathcal{M}_d . For any point $x_d \in \mathcal{M}_d$, there exists a homeomorphic local parameterization $l_d : \mathcal{O} \subset \mathbb{R}^{p_d} \mapsto \mathcal{V} \cap \mathcal{M}_d \subset \mathbb{R}^{m_d}$, where \mathcal{O} is an open set of

\mathbb{R}^{p_d} , and \mathcal{V} is an open set of \mathbb{R}^{m_d} . We denote the local coordinates corresponding to x_d by $\gamma^{(d)} = l_d^{-1}(x_d) \in \mathcal{O}$. Then the tangent space $T_{x_d}(\mathcal{M}_d)$ at x_d has a basis given by the vectors $\{\frac{\partial l_d}{\partial \gamma_i^{(d)}}(\gamma^{(d)})\}_{i=1}^{p_d}$, which are elements in \mathbb{R}^{m_d} . The induced metric g_d at x_d can be represented by a $p_d \times p_d$ matrix with elements defined by $[G^{(d)}(\gamma^{(d)})]_{ij} = \langle \frac{\partial l_d}{\partial \gamma_i^{(d)}}(\gamma^{(d)}), \frac{\partial l_d}{\partial \gamma_j^{(d)}}(\gamma^{(d)}) \rangle$, such that for any $u_1, u_2 \in T_{x_d}(\mathcal{M}_d)$, $g_d(u_1, u_2) = u_1^T G^{(d)}(\gamma^{(d)}) u_2$. The LBO acting on a smooth function $v_d : \mathcal{M}_d \mapsto \mathbb{R}$ is then defined as

$$\Delta_{\mathcal{M}_d}[v_d](x_d) = \frac{1}{\sqrt{\det G^{(d)}(\gamma^{(d)})}} \sum_{i,j=1}^{p_d} \frac{\partial}{\partial \gamma_i^{(d)}} \left(\sqrt{\det G^{(d)}(\gamma^{(d)})} [G^{(d)}(\gamma^{(d)})]_{ij}^{-1} \frac{\partial v_d}{\partial \gamma_j^{(d)}}(l_d(\gamma^{(d)})) \right). \quad (1)$$

Extending this definition to the manifold $\Omega = \times_{d=1}^D \mathcal{M}_d$, we utilize the fact that the LBO on a product manifold is the sum of the LBOs of its component manifolds: $\Delta_{\Omega} = \sum_{d=1}^D \Delta_{\mathcal{M}_d}$ (Canzani, 2013). Thus, for a smooth function $v : \Omega \rightarrow \mathbb{R}$, the LBO is given by

$$\Delta_{\Omega}[v](x_1, \dots, x_D) = \sum_{d=1}^D \frac{1}{\sqrt{\det G^{(d)}(\gamma^{(d)})}} \times \sum_{i,j=1}^{p_d} \frac{\partial}{\partial \gamma_i^{(d)}} \left(\sqrt{\det G^{(d)}(\gamma^{(d)})} [G^{(d)}(\gamma^{(d)})]_{ij}^{-1} \frac{\partial v}{\partial \gamma_j^{(d)}}(x_1, \dots, l_d(\gamma^{(d)}), \dots, x_D) \right). \quad (2)$$

Note that in this expression, v is considered as a function of all variables (x_1, \dots, x_D) , and when differentiating with respect to $\gamma_j^{(d)}$, all other variables x_i for $i \neq d$ are treated as constants.

2.2 Statistical Model and Problem Formulation

Let $o = \{\mathbf{x}_1, \mathbf{x}_2, \dots, \mathbf{x}_n\} \subset \Omega$, where $\mathbf{x}_i := (x_{1i}, x_{2i}, \dots, x_{Di}) \in \Omega$, be an iid set of observations from density function $f \in \mathcal{H}$, with $\mathcal{H} := \{f : \Omega \mapsto \mathbb{R}^+ : \int_{\Omega} f d\omega = 1\}$. In this work, we focus on likelihood-based estimation of f from o . To handle the positivity constraint on f , we adopt a standard log transformation approach and target the log-density, denoted here as $v = \log f$, with the corresponding transformed function space $\tilde{\mathcal{H}} = \{v : \Omega \mapsto \mathbb{R} : \int \exp(v) d\omega = 1\}$. As v is infinite dimensional, its estimation from finite samples o requires regularization to avoid undesirable behavior, e.g., pathological estimates converging to a mixture of Dirac functions centered on each observation. A commonly used

regularizer for function approximation is the *roughness penalty*, which controls smoothness by penalizing the L^2 -norm of the Laplacian operator applied to the candidate function. Since the LBO generalizes the Laplacian to smooth manifold domains, it naturally serves as a basis for defining a roughness penalty in our context. Formally, assuming $v : \Omega \mapsto \mathbb{R}$ is smooth, we consider penalties of the form:

$$R_\tau(v) = \tau \int_{\Omega} [\Delta_{\Omega} v]^2 d\omega. \quad (3)$$

Putting this all together, we aim to find the function v that maximizes the penalized log-likelihood:

$$\begin{aligned} \hat{v} &= \arg \max_{v \in \tilde{\mathcal{H}}} \log p(o|v) - R_\tau(v) = \arg \max_{v \in \tilde{\mathcal{H}}} \sum_{i=1}^n v(\mathbf{x}_i) - R_\tau(v) \\ &= \arg \max_{v \in C^\infty(\Omega)} \sum_{i=1}^n v(\mathbf{x}_i) - n \int_{\Omega} \exp(v) d\omega - R_\tau(v), \end{aligned} \quad (4)$$

where $\tau > 0$ is the regularization strength. The equality in the second line of (4) is a consequence of Theorem 3.1 in (Silverman, 1982), which is deployed here in order to remove the integrability constraint in $\tilde{\mathcal{H}}$ from the optimization problem. Notably, (4) can be alternatively motivated from a Bayesian perspective as a MAP estimator under a function space smoothness prior proportional to $\exp(-R_\tau(v))$ (Good and Gaskins, 1971). However, as this work focuses solely on point estimation, the Bayesian framing is incidental.

Remark 1. *The optimization problem in (4) provides an equivalent formulation for intensity function estimation. Specifically, assuming $o \sim O$ and O is an inhomogeneous Poisson process, the penalized maximum likelihood intensity function estimate is simply $n\hat{f}$. For more details on this relationship, we refer the reader to Appendix B of Begu et al. (2024).*

3 Deep Neural Field for Product Manifold Density Modeling

In this section, we propose our representation model for the log-density and study its expressive power. To avoid the severe computational issues of nonparametric estimators for functions over multidimensional domains, we restrict our attention to parametric models for v . That is, we seek solutions \hat{v}_θ to (4), parameterized by some finite dimensional vector θ . Traditional parametric approaches often lack flexibility (single index models, additive models) or scale poorly with domain dimensionality (tensor product basis). Alternatively,

deep neural network-based parameterizations, commonly referred to as neural fields (NF) or implicit neural representations (INRs), have gained significant recent attention for their ability to provide high-fidelity, parameter-efficient representations of continuous functions. These properties have led to their widespread application in computer vision (Sitzmann et al., 2020; Tancik et al., 2020; Xie et al., 2022), shape representation (Takikawa et al., 2021), and physics-based problems (Raissi et al., 2019).

In this work, we develop a NF-based approach for modeling the log-density v . The core architecture is a fully connected multi-layer perceptron (MLP), defined by:

$$\begin{aligned} \mathbf{h}^{(0)} &= \boldsymbol{\eta}(\mathbf{x}) \\ \mathbf{h}^{(l)} &= \alpha^{(l)}(\mathbf{W}^{(l)}\mathbf{h}^{(l-1)} + \mathbf{b}^{(l)}), \quad l = 1, \dots, L-1 \\ v_{\boldsymbol{\theta}}(\mathbf{x}) &:= \mathbf{W}^{(L)}\mathbf{h}^{(L-1)}, \end{aligned} \tag{5}$$

where $\mathbf{x} := (x_1, \dots, x_D) \in \Omega$, $\boldsymbol{\theta} := (\text{vec}(\mathbf{W}^{(1)}), \dots, \text{vec}(\mathbf{W}^{(L)}), \text{vec}(\mathbf{b}^{(1)}), \dots, \text{vec}(\mathbf{b}^{(L)})) \in \Theta$ consists of the weights $\mathbf{W}^{(l)} \in \mathbb{R}^{H_l \times H_{l-1}}$ and biases $\mathbf{b}^{(l)} \in \mathbb{R}^{H_l}$ of the network, $\alpha^{(l)}$ are the activation functions, and $\boldsymbol{\eta} : \Omega \mapsto \mathbb{R}^{H_0}$ is multivariate function on multidimensional domain Ω . An illustration of the proposed MLP is provided in supplemental Figure S1.

We complete the definition of our functional model (5) by formally specifying the encoding function $\boldsymbol{\eta}$ in Section 3.1 and the activation functions $\alpha^{(l)}$, along with the weight initialization scheme, in Section 3.2. In Section 3.3, we study the effect of these custom design choices for the special case of hypertoroidal domains, demonstrating a strong trade-off between expressive power and parameter efficiency of (5), while avoiding the computational curse of dimensionality.

3.1 Random Laplace-Beltrami Eigenfunction Encoding

We now outline the construction of the encoding function $\boldsymbol{\eta}$. To avoid computational issues associated with direct operations on the full product space, our design uses randomized basis functions formed from products of the eigenfunctions of the LBO on the marginal manifolds. While this provides a simple computationally efficient way to design a basis for a potentially high-dimensional product manifold, the encoding functions resulting from this approach are always separable, which may be undesirable. Therefore, we introduce an optional step that rotates the eigenbasis within each eigenspace, enabling the formation of

non-separable eigenfunctions for a more flexible encoding, while maintaining the frequency of the original basis.

For a smooth Riemannian manifold \mathcal{M} , the eigenfunctions $\phi_k : \mathcal{M} \mapsto \mathbb{R}$ of the LBO are defined as the solutions to the operator equation

$$\Delta_{\mathcal{M}}\phi_k = -\lambda_k\phi_k, \quad k = 1, 2, \dots \quad (6)$$

These eigenfunctions form an orthonormal basis for the space $L^2(\mathcal{M})$, with the eigenvalues λ_k forming a non-decreasing sequence of non-negative scalars, analogous to the frequencies in Fourier analysis. Consequently, finite rank- K sets $\{\phi_k\}_{k=1}^K$ are often used as basis systems for function representation. For instance, popular basis systems such as the Fourier series and the spherical harmonics are special cases when $\mathcal{M} := \mathbb{S}^1$ and $\mathcal{M} := \mathbb{S}^2$, respectively. For general manifolds, these eigenfunctions typically cannot be analytically derived, requiring the use of numerical methods to approximate the solutions to (6) (Reuter et al., 2009).

For a product manifold $\Omega = \times_{d=1}^D (\mathcal{M}_d, g_d)$ equipped with the product metric $\sum_{d=1}^D g_d$, the LBO decomposes as $\Delta_{\Omega} = \sum_{d=1}^D \Delta_{\mathcal{M}_d}$. Denote the multi-index $\mathbf{i} = (i_1, \dots, i_D)$. The functions defined by the tensor product of the marginal eigenfunctions, $\psi_{\mathbf{i}} := \prod_{d=1}^D \phi_{i_d}$, form a complete basis of eigenfunctions for $L^2(\Omega)$, with corresponding eigenvalues $\sum_{d=1}^D \lambda_{i_d}$, where λ_{i_d} is the marginal eigenvalue for ϕ_{i_d} (Canzani, 2013). Drawing from classical function approximation theory, a seemingly natural way to define $\boldsymbol{\eta}$ in (6) is to use the basis functions formed by a finite tensor product of marginal eigenfunctions. Specifically, denote $\lambda_{d,\max} \in \mathbb{R}^+$ as the truncation of the spectrum along the d 'th domain and define the multi-index set $\mathcal{I}_{\lambda} = \{\mathbf{i} : \sum_{d=1}^D \lambda_{i_d} = \lambda, \lambda_{i_d} \leq \lambda_{d,\max}, \forall d\}$. Define the function $\boldsymbol{\psi}_{\lambda} := (\psi_{\mathbf{i}} : \psi := \prod_{d=1}^D \phi_{i_d}, \mathbf{i} \in \mathcal{I}_{\lambda}) : \Omega \mapsto \mathbb{R}^{s_{\lambda}}$, where s_{λ} is the multiplicity of \mathcal{I}_{λ} . With slight abuse of notation, the collection of tensor product basis functions is given by $\bigcup_{\lambda \leq \lambda_{\max}} \boldsymbol{\psi}_{\lambda}$, where $\lambda_{\max} = \sum_{d=1}^D \lambda_{d,\max}$. However, as the number of these basis functions grows exponentially with D , this choice causes the column space of the first-layer weight matrix $\mathbf{W}^{(1)}$ in (5) to grow at the same exponential rate, resulting in significant computational challenges during network training. To avoid this manifestation of the computational curse of dimensionality, a different approach is necessary.

Inspired by random Fourier feature encodings for functional data in \mathbb{R}^D , we propose to randomly sample without replacement K LBO eigenfunctions ψ_1, \dots, ψ_K from the tensor

product set $\bigcup_{\lambda \leq \lambda_{\max}} \boldsymbol{\psi}_\lambda$ and take $\boldsymbol{\eta}(x_1, \dots, x_D) := (\psi_1(x_1, \dots, x_D), \dots, \psi_K(x_1, \dots, x_D))^\top$. Since K is an architecture hyperparameter and can be chosen independently of D , this approach avoids the curse of dimensionality associated with using the full tensor product basis system. We establish the strong expressive power of this choice of $\boldsymbol{\eta}$ theoretically in Section 3.3 and validate it empirically through simulations in Section 5.

When using the raw tensor products, all basis functions in the encoding $\boldsymbol{\eta}$ are *separable*, that is, they can be written as products over the marginal domains. To gain more flexibility, we introduce an optional basis rotation step. Specifically, let $\mathbf{A}_\lambda \in \mathbb{R}^{s_\lambda \times s_\lambda}$ be an orthogonal matrix, then it is easy to show that $\tilde{\boldsymbol{\psi}}_\lambda = \mathbf{A}_\lambda \boldsymbol{\psi}_\lambda$ is a basis for the same eigenspace: $\text{span}(\boldsymbol{\psi}_\lambda)$. When $\mathbf{A}_\lambda \neq \mathbf{I}$, the basis functions $\tilde{\boldsymbol{\psi}}_\lambda$ are *non-separable*, meaning they cannot be written as a product of functions over the marginal domains \mathcal{M}_d . Although in theory functions $\boldsymbol{\psi}_\lambda$ and $\tilde{\boldsymbol{\psi}}_\lambda$ span the same space, we have empirically observed that the choice of basis can have a significant impact on the algorithmic convergence (the spectral bias), and hence can be tuned to accelerate the training of (5). For further discussion and empirical analysis of this effect, see supplemental Section S3.3 and S5.1.3. Putting this together, we define the first layer encoding function as:

$$\begin{aligned} \psi_1, \dots, \psi_K &\stackrel{u.w.o.r.}{\sim} \bigcup_{\lambda \leq \lambda_{\max}} \mathbf{A}_\lambda \boldsymbol{\psi}_\lambda \\ \boldsymbol{\eta}(x_1, \dots, x_D) &:= (\psi_1(x_1, \dots, x_D), \dots, \psi_K(x_1, \dots, x_D))^\top, \end{aligned} \tag{7}$$

where *u.w.o.r.* indicates uniform sampling w/o replacement.

In summary, the first layer encoding function $\boldsymbol{\eta}$ consists of randomly sampled products of marginal LBO eigenfunctions that can be optionally rotated. The random sampling of LBO eigenfunctions is essential in overcoming the computational curse of dimensionality as D and $|\mathcal{M}_d|$ increase, while preserving strong expressive power.

3.2 Hidden Layer Activations and Initialization

To complete the definition of our deep intensity estimator (5), we define the activation functions $\alpha^{(l)}$ as sinusoidal functions for all hidden layers, i.e., $\alpha^{(l)}(\cdot) := \sin(\cdot)$, $\forall l$. Despite historical reticence in using non-monotonic, periodic activations due to observed pathological effects on the loss surface (Parascandolo et al., 2017) and perceived difficulty in

training (Lapedes and Farber, 1987), Sitzmann et al. (2020) demonstrate that with a carefully designed weight initialization scheme—where the output distribution at initialization is independent of the network depth and the input to each hidden activation is a standard normal—deep networks with hidden sinusoidal activations can be trained stably. Empirical results indicate that sinusoids with proper initialization can substantially improve convergence speed compared to traditional activations (Faroughi et al., 2024), a finding also supported by our experiments.

3.3 Expressive Power of the Neural Field Architecture

The ultra-high-dimensionality of the parameter space Θ and significant non-linearities make theoretic analysis of deep neural network estimators notoriously challenging. As a result, the types of functions that (5) has the capacity to express are not immediately clear in the general case. In what follows, we consider the special case of $\mathcal{M}_d = \mathbb{S}^1$, i.e. Ω is a D -torus, and establish the theory of the representation space, showing that when the model (5) is sufficiently deep, it is flexible enough to capture very high-frequency details of the underlying function.

Before introducing the theorem, we provide some necessary background. We can parameterize \mathbb{S}^1 by intrinsic coordinates $[0, 2\pi)$, with 0 and 2π identified. Denote $x \in \mathbb{S}^1$, then a general solution to (6) is given by: $\phi_{2i-z}(x) = \frac{1}{\sqrt{\pi}} \cos\left(ix - \frac{z\pi}{2}\right)$, $i \in \mathbb{Z}_+$, $z \in \{0, 1\}$, with eigenvalues i^2 for $i \neq 0$, $\phi_0(x) = \frac{1}{\sqrt{2\pi}}$ with eigenvalue zero, and z controls the choice between sin and cos. See Section S2.1 for a derivation. Forming the tensor products, the non-trivial eigenfunctions on \mathbb{T}^D with maximum marginal eigenvalue $i_{d,max}^2$ are given by

$$\psi(\mathbf{x}) \in \left\{ \pi^{-D/2} \prod_{d=1}^D \cos(i_d x_d - \frac{z_d \pi}{2}) : 1 \leq i_d^2 \leq i_{d,max}^2, (z_1, \dots, z_D) \in \{0, 1\}^D \right\}, \quad (8)$$

where $\mathbf{x} := (x_1, \dots, x_D) \in \mathbb{T}^D$, with associated (non-zero) eigenvalues $\lambda = \sum_{d=1}^D i_d^2$.

Without loss of generality, we let $\mathbf{A}_\lambda = \mathbf{I}$, $\forall \lambda$, so $\boldsymbol{\eta}$ contains K randomly sampled elements without replacement from the set (8). Denote the k -th sampled tensor product basis function as

$$\psi_k(\mathbf{x}) = \prod_{d=1}^D \phi_{i_{k,d}}(x_d) = \pi^{-D/2} \prod_{d=1}^D \cos(i_{k,d} x_d - z_{k,d} \pi / 2), z_{k,d} \in \{0, 1\}, \quad (9)$$

where $1 \leq k \leq K$ serves as the index for the k -th basis function, and $(i_{k,1}, \dots, i_{k,D}) \in \times_{d=1}^D \{1, \dots, i_{d,max}\}$ is the corresponding *frequency vector*. The following theorem provides a compact interpretable form for the types of functions that can be represented by the architecture (5) for the case of \mathbb{T}^D .

Theorem 1. *Assume all weights and biases are bounded: $\max_{1 \leq l \leq L-1} |\mathbf{b}^{(l)}| < C_b$ and $\max_{1 \leq l \leq L-1} |\mathbf{W}^{(l)}| < C_w$ with $0 < C_b, C_w < \infty$. Let $\Omega = \mathbb{T}^D = \times_{d=1}^D \mathbb{S}^1$, $v_{\theta} : \mathbb{T}^D \rightarrow \mathbb{R}$ be an NF of the form (5), with $\alpha^{(l)}(v) = \sin(v)$ for $1 \leq l \leq L-1$, and $\boldsymbol{\eta} : \mathbb{T}^D \mapsto \mathbb{R}^K$ whose k -th element is defined as (9). Denote frequency vector set $\mathcal{W}_k = \{(i_{k,1}, \pm i_{k,2}, \dots, \pm i_{k,D})\}$, for $k = 1, \dots, K$. Then the NF v_{θ} can be expressed as*

$$v_{\theta}(\mathbf{x}) = \sum_{\mathbf{w}' \in \mathcal{H}^{(L)}} \beta_{\mathbf{w}'} \cos(\langle \mathbf{w}', \mathbf{x} \rangle + b_{\mathbf{w}'}) + \epsilon, \quad \mathcal{H}^{(L)} = \left\{ \tilde{\mathbf{w}} = \sum_{k=1}^K c_k \mathbf{w}_k \mid c_k \in \mathcal{A}^{(L)}, \mathbf{w}_k \in \mathcal{W}_k \right\},$$

where $\mathcal{A}^{(L)} = \{c_k = \prod_{l=1}^L c_k^{(l)} \mid c_k^{(l)} \in \mathcal{A}\}$, with $\mathcal{A} = \{c_k^{(l)} \in \{n_k, n_k - 2, \dots, -(n_k - 2)\} \mid \sum_{k=1}^K n_k \in \{1, \dots, M_{\epsilon}\}, n_k \in \mathbb{N}\}$, and $M_{\epsilon} = \min\{m : C_w^{L-2}(C_w + C_b)^{2m+3}/(2m+3)! < \epsilon\}$, $\epsilon > 0$ is a constant and the $\beta_{\mathbf{w}'}$ are complicated functions of θ .

Note that the cardinality of \mathcal{A} , $|\mathcal{A}| \geq M_{\epsilon}$, thus, the cardinality of $\mathcal{H}^{(L)}$ is of similar order to M_{ϵ}^L , and hence grows very quickly with respect to the number of hidden layers L . Therefore we see that, for the special case of \mathbb{T}^D , the network (5) is approximately equivalent to an expansion over a large set of sinusoidal basis functions, with frequencies in $\mathcal{H}^{(L)}$ that are scaled versions of those used to form $\boldsymbol{\eta}$, and whose expansion coefficients are determined by the network parameters. We note that similar representation results have been identified for several types of NF architectures for representing Euclidean functions (Fathony et al., 2021; Yüce et al., 2022).

4 Estimation and Computational Details

4.1 Scalable Stochastic Gradient Algorithm

Under the deep network model outlined in Section 3, the parametric form of the optimization problem (4) is given by:

$$\hat{\theta} := \arg \max_{\theta \in \Theta} \mathcal{L}(o, \theta) = \arg \max_{\theta \in \Theta} \left(\frac{1}{n} \sum_{i=1}^n v_{\theta}(\mathbf{x}_i) - \int_{\Omega} \exp(v_{\theta}) d\omega - R_{\tau}(v_{\theta}) \right). \quad (10)$$

In general, optimization problems for deep network parameters are both high dimensional and highly non-convex and, therefore, are not solved globally. Instead, local solutions are found using stochastic gradient-based procedures (Kingma and Ba, 2015), with gradients computed via backpropagation.

A potential complexity arises in our case because the normalization and penalty terms in (10) involve integration over Ω , which in general is analytically intractable. Numerical approximation using quadrature rules, an effective approach in lower-dimensional settings (Ferraccioli et al., 2021), must be avoided as it reintroduces the curse of dimensionality, with the total number of quadrature points being exponential in D . Instead, recall that stochastic gradient-based optimization procedures require only an unbiased estimate of the objective function’s gradient (Bottou et al., 2018). Leveraging this fact, the following proposition establishes that the necessary gradients can be computed while avoiding the computational curse of dimensionality.

Proposition 1. *Let $\text{Vol}(\Omega) := \int_{\Omega} d\omega$ and define*

$$\begin{aligned} \mathbf{a}^b(\boldsymbol{\theta}) &:= \frac{1}{b} \sum_{i=1}^b \frac{\partial}{\partial \boldsymbol{\theta}} v_{\boldsymbol{\theta}}(x_{1i}, \dots, x_{Di}), & \mathbf{b}^{q_1}(\boldsymbol{\theta}) &:= \frac{\text{Vol}(\Omega)}{q_1} \sum_{j=1}^{q_1} \frac{\partial}{\partial \boldsymbol{\theta}} \exp(v_{\boldsymbol{\theta}}(x_{1j}, \dots, x_{Dj})) \\ \mathbf{c}_{\tau}^{q_2}(\boldsymbol{\theta}) &:= \tau \frac{\text{Vol}(\Omega)}{q_2} \sum_{l=1}^{q_2} \frac{\partial}{\partial \boldsymbol{\theta}} [\Delta_{\Omega} v_{\boldsymbol{\theta}}(x_{1l}, \dots, x_{Dl})]^2, \end{aligned} \tag{11}$$

where $b \leq n$ is the size of a uniformly sampled data batch from o , and q_1, q_2 are the Monte Carlo sample sizes with points sampled uniformly over Ω . Then

$$\mathbb{E}[\mathbf{a}^b(\boldsymbol{\theta}) - \mathbf{b}^{q_1}(\boldsymbol{\theta}) - \mathbf{c}_{\tau}^{q_2}(\boldsymbol{\theta})] = \frac{\partial}{\partial \boldsymbol{\theta}} \mathcal{L}(o, \boldsymbol{\theta}).$$

As a result of proposition 1, if the terms in Equation 11 can be quickly computed, the solution to (10) can be approximated using a batch stochastic gradient ascent procedure. The gradients required for $\mathbf{a}^b(\boldsymbol{\theta})$ and $\mathbf{b}^{q_1}(\boldsymbol{\theta})$ can be formed efficiently using backpropagation. However, forming $\mathbf{c}_{\tau}^{q_2}(\boldsymbol{\theta})$ is complicated by the presence of the manifold differential operator Δ_{Ω} . To handle this term, we consider two cases.

For certain product manifolds, definition (2) simplifies considerably. For instance, in the case of the D -dimensional torus $\mathbb{T}^D = \times_{d=1}^D \mathbb{S}^1$, the metric tensor components and their determinants become constants, and the LBO reduces to a sum of standard Laplacians on each circle component (see Supplemental Section S2.1). In such cases, the network (5) can

be defined directly on the intrinsic coordinates $(\gamma^{(1)}, \dots, \gamma^{(D)})$, and $\Delta_\Omega[v]$ computed using automatic differentiation (Baydin et al., 2018).

Alternatively, in applications involving more complex manifolds with many local charts, forming (2) may become cumbersome and challenging. In such cases, it may be more convenient to work directly with the extrinsic (Euclidean) coordinates (Harlim et al., 2023). The following proposition provides an alternative computational form for point-wise evaluation of the LBO of a smooth function v that avoids the explicit use of local coordinates.

Proposition 2. *Let $v : \Omega \mapsto \mathbb{R}$ be a smooth function on the product manifold Ω . Let $\{t_1^{(d)}, \dots, t_{p_d}^{(d)}\}$ be a set of orthogonal basis vectors in \mathbb{R}^{m_d} that span $T_{x_d}(\mathcal{M}_d)$ (tangent space at $x_d \in \mathcal{M}_d$). Define the matrices $\mathbf{P}^{(d)} = \sum_{i=1}^{p_d} t_i^{(d)} t_i^{(d)\top} \in \mathbb{R}^{m_d \times m_d}$ and the block diagonal matrix $\mathbf{P} = \text{BlockDiag}(\mathbf{P}^{(1)}, \dots, \mathbf{P}^{(D)})$. Then the Laplace-Beltrami operator of v is given by*

$$\Delta_\Omega[v](\mathbf{x}) = \sum_{i=1}^M \mathbf{P}_{i,\cdot} \mathbf{H}_{\mathbb{R}^M}[v](x_1, \dots, x_D) \mathbf{P}_{i,\cdot}^\top, \quad (12)$$

where $M = \sum_{d=1}^D m_d$, $\mathbf{H}_{\mathbb{R}^M}$ is the standard Hessian in \mathbb{R}^M and $\mathbf{P}_{i,\cdot}$ is the i -th row of \mathbf{P} .

Equation (12) implies that if we can efficiently calculate i) the second order derivatives of v in the ambient Euclidean space and ii) the basis vectors to form $\mathbf{P}^{(d)}$, we can construct the differential operators of interest efficiently. Regarding i), the required Euclidean Hessian can be calculated via automatic differentiation. The ease of ii) depends on the manifold in question. For some manifolds of interests, e.g. \mathbb{S}^p , closed form solutions exist and hence can be calculated rapidly. In the general case, it is common for complicated manifolds to be approximated using triangulations (or their higher dimensional analogs). In such situations, the tangent basis can be approximated directly using the triangulation vertices.

Algorithm 1 provides pseudocode for our stochastic gradient ascent based estimation procedure. In general, proving the convergence of the iterates in Algorithm 1 to a stationary point of (10) requires some additional assumptions on $\mathcal{L}(o, \boldsymbol{\theta})$ that are difficult to verify, e.g. globally Lipschitz gradients (Ghadimi and Lan, 2013). Empirically, we found convergence to be robust for simple learning rate sequences, provided that τ was large enough to avoid the case of unbounded or nearly unbounded likelihoods. For additional details on the algorithm and practical implementation guidance, please refer to Supplemental Section S3.2.

Algorithm 1 Mini-batch Stochastic Gradient Ascent Estimator

- 1: **Input** non-negative sequence of learning rates $\{w_t\}$, architecture hyperparameters for (5), batch sizes b , MC sample sizes q_1, q_2 , regularization strength τ
 - 2: Set $\boldsymbol{\eta} := (\psi_1, \dots, \psi_K)^\top$ by sampling $\{\psi_i\}$ via (7)
 - 3: Initialize $\boldsymbol{\theta}^i$ using scheme from Sitzmann et al. (2020)
 - 4: **for** $t = 1, \dots, T$ **do**
 - 5: **for** $l = 1, \dots, \lfloor \frac{n}{b} \rfloor$ **do**
 - 6: Sample mini-batch $\{\mathbf{x}_i\}_{i=1}^b$ uniformly from o
 - 7: Sample $\{\mathbf{x}_j\}_{j=1}^{q_1}, \{\mathbf{x}_l\}_{l=1}^{q_2} \stackrel{iid}{\sim} \text{Unif}(\Omega)$
 - 8: Calculate $\frac{\partial}{\partial \boldsymbol{\theta}} \widehat{\mathcal{L}}(o, \boldsymbol{\theta}^i)$ using Proposition 1.
 - 9: Update $\boldsymbol{\theta}^c = \boldsymbol{\theta}^i - w_t \frac{\partial}{\partial \boldsymbol{\theta}} \widehat{\mathcal{L}}(o, \boldsymbol{\theta}^i)$
 - 10: Set $\boldsymbol{\theta}^i = \boldsymbol{\theta}^c$
 - 11: **Return:** $\widehat{\boldsymbol{\theta}} := \boldsymbol{\theta}^c$
-

4.2 Hyperparameter Selection

As is typical for deep neural network based estimators, Algorithm 1 involves many hyperparameters that require tuning. Evaluating the quality of a given hyperparameterization necessitates a data-driven criterion. Towards this end, we first partition the observed points into training o_T and validation o_V sets. We estimate $\widehat{\boldsymbol{\theta}}$ using Algorithm 1 with o_T for each candidate hyperparameterization, and then calculate criterion

$$C(\widehat{\boldsymbol{\theta}}) = \|f_{\widehat{\boldsymbol{\theta}}}\|_{L^2(\Omega)}^2 - \frac{2}{|o_V|} \sum_{\mathbf{x}_i \in o_V} f_{\widehat{\boldsymbol{\theta}}}(\mathbf{x}_i), \quad (13)$$

with the integral estimated using Monte-Carlo integration. The criteria (13) corresponds to a shifted approximation of the integrated squared error (ISE) of the density estimator (Hall and Marron, 1987).

In theory, criterion (13) can be utilized within various algorithms for hyperparameter selection. The design of such algorithms remains a challenging and active area of research in the machine learning community, due to the high dimensionality of the hyperparameter spaces and high cost of computing estimators (Yu and Zhu, 2020). After experimenting with modern approaches to jointly optimize over many hyperparameters (Snoek et al., 2012), we found that a simple two stage approach worked best. In this approach, all hyperparameters except for τ are first fixed to values deemed reasonable based on the

literature and exploratory experimentation. The parameter τ was then selected over a grid $\tau_1 < \tau_2 < \dots < \tau_S$ via: $\tau = \arg \min_{\tau_s \in \{\tau_1, \dots, \tau_S\}} C(\widehat{\boldsymbol{\theta}}_{\tau_s})$, where $\widehat{\boldsymbol{\theta}}_{\tau_s}$ is estimated from Algorithm 1 with o_T and τ_s . This approach proved effective, as Algorithm 1 was found to be particularly sensitive to the choice of τ .

We conclude this section with a few practical guidelines for setting the remaining hyper-parameters. For network size, we found that operating in or near the over-parameterized regime is effective, with the total number of network parameters ranging from at least half to twice n . A large data batch size is recommended, typically between $n/2$ and $n/4$, which aligns with empirical findings reported for training Euclidean NFs on Gaussian data (Dupont et al., 2022). The Monte Carlo sample size q_1 can typically be set relatively high, however, a large q_2 may significantly slow training, particularly when automatic differentiation is employed to approximate the roughness penalty (see Supplemental Section S3.2 for alternative derivative calculation strategies). We recommend setting the encoding basis rank K equal to the width of the first layer and increasing the maximum frequency of the marginal basis as the dimensionality increases. Finally, criteria (13) can also be used for early stopping, that is, selecting T , by monitoring its value on a small validation set and terminating Algorithm 1 when it plateaus, as demonstrated in Supplemental Section S5.1.4.

5 Empirical Evaluation

5.1 Synthetic Data Analysis

5.1.1 Simulation Setup

We evaluate the recovery of the target density f on the (hyper)-torus \mathbb{T}^D using simulated data. We focus on the hyper-toroidal case because it allows for easier definition and sampling of non-separable anisotropic density functions, and because there are standard competing alternatives available. We consider $\Omega = \mathbb{T}^2$ ($D = 2$) and \mathbb{T}^4 ($D = 4$) cases to study the performance of the method on both (relatively) low and high-dimensional domains. The true density functions are defined using mixtures of anisotropic wrapped normal distributions (Mardia and Jupp, 2009). For \mathbb{T}^2 , the density is defined as an equally weighted mixture of three anisotropic components, as shown in the top left panel of Figure 2. For \mathbb{T}^4 , the density is an equally weighted mixture of 5 anisotropic components.

$n = 10,000$ and $n = 100,000$ observations are simulated for \mathbb{T}^2 and \mathbb{T}^4 , respectively. The MATLAB library *libDirectional* was used for defining and sampling the mixture model (Kurz et al., 2019). 20 replications were formed for each dataset. For more details on the synthetic data generation, see supplemental Section S5.

The eigenfunctions of the LBO on \mathbb{S}^1 using intrinsic (polar) coordinates are the Fourier functions with discrete frequencies. For both \mathbb{T}^2 and \mathbb{T}^4 , we set the marginal maximum frequencies $\lambda_{d,max} = 10$, $d = 1, \dots, D$ and take $K = 128$. To form the first layer encoding $\boldsymbol{\eta}$, for \mathbb{T}^2 , we sample the separable tensor product eigenfunctions. For \mathbb{T}^4 , we employ the augmented approach outlined in Section 3.1 and use non-separable eigenfunctions formed via predefined rotation of the separable eigenfunctions (see supplemental Section S5.1.3 for more details). The width of all hidden layers is set to 128. For \mathbb{T}^2 , we use a depth $L = 3$, whereas for \mathbb{T}^4 , we increase the depth to $L = 4$ to reflect the increased dimensionality of the problem. To calculate the gradients in (11), we let batch size $b = n/2$, and set $q_1 = q_2 = 1,024$ to sample quadrature points using quasi-Monte Carlo over $[-\pi, \pi]^D$ (Owen, 1998). The intrinsic form of the LBO is used for the roughness penalty computation. For the \mathbb{T}^2 case, we train for 10,000 epochs with a fixed learning rate of 10^{-5} . In the \mathbb{T}^4 case, we use a cyclic learning rate under the triangular policy (Smith, 2017), as described in Supplemental Section S3.2, where the learning rate cycles between a maximum and minimum of 10^{-3} and 10^{-5} , respectively, every 5,000 epochs, for 10,000 total epochs. For selecting τ , we use a held-out validation set of size $0.05n$ and consider a logarithmically spaced grid of candidate solutions from 10^{-5} to 10^1 .

We compare our method, from here on referred to as Neural Product Manifold Density (NeuroPMD), to a couple standard density estimators. I) a product kernel density estimation (KDE) with marginal kernels taken to be von Mises densities. We assume a common bandwidth for all marginal domains to avoid complex multidimensional bandwidth selection issues. The bandwidth is selected via 5-fold cross validation using the approximate ISE criteria (13). II) Basis expansion over the tensor product eigenfunctions (TPB), i.e. model $v(x_1, \dots, x_D) = \sum_{i_1, \dots, i_D} c_{i_1, \dots, i_D} \phi_{i_1}(x_1) \cdots \phi_{i_D}(x_D)$. The expansion coefficients $\{c_{i_1, \dots, i_D}\}$ are estimated using stochastic gradient ascent on the penalized log-likelihood (4), which has been used for basis function density estimators in the literature (Ferraccioli et al., 2021), and can be guaranteed to converge under some standard conditions (see Supplemen-

tal Section S4 for more details). The hyperparameter τ for the TBP estimator was selected using the scheme outlined in Section 4.2, applied independently to all replications for \mathbb{T}^2 . For \mathbb{T}^4 , due to the computational challenges of estimating the tensor-product basis in this high-dimensional domain, the full hyperparameter optimization was performed for a single replication to select τ , which was then fixed for the remaining replications to manage the computational cost. For \mathbb{T}^2 , the marginal maximum frequencies are also set as $\lambda_{d,max} = 10 \forall d$. However, due to the curse of dimensionality, applying this strategy to \mathbb{T}^4 results in a basis expansion with $(2(10) + 1)^4 = 194,481$ unknown parameters, the estimation of which proved to be prohibitively costly for our experiments. Therefore, we set the marginal maximum frequencies to $\lambda_{d,max} = 7 \forall d$, resulting in $(2(7) + 1)^4 = 50,625$ coefficients. This choice was made to approximately match the parameter count of the \mathbb{T}^4 NeuroPMD architecture, which has $3(128^2 + 128) + 128 + 1 = 49,665$ parameters. We also compared our method to a “vanilla” MLP with ReLU activations and the identity encoding function: $\boldsymbol{\eta}(\mathbf{x}) = \mathbf{x}$. However, this baseline approach did not achieve competitive performance compared to any of the alternatives; detailed results are provided in Supplemental Section S5.1.2

To evaluate the estimation performance of all methods, we use two metrics: the normalized $L^2(\Omega)$ error (nISE) and the Fisher-Rao metric (FR), both defined with respect to the true density function, as follows:

$$\text{nISE}(\hat{f}) = \left\| f - \hat{f} \right\|_{L^2(\Omega)}^2 / \|f\|_{L^2(\Omega)}^2, \quad \text{FR}(\hat{f}) = \cos^{-1} \left(\left\langle \sqrt{f}, \sqrt{\hat{f}} \right\rangle_{L^2(\Omega)} \right).$$

The integrals required for these metrics are approximated differently depending on the dimensionality of the problem. For the relatively low-dimensional case of \mathbb{T}^2 , we use the tensor product of dense marginal grids, while for the higher-dimensional case of \mathbb{T}^4 , we rely on Monte Carlo integration. It is worth noting that the FR is the L^2 Riemannian distance on \mathbb{S}^∞ , the unit sphere in the space of $L^2(\Omega)$ functions. The square-root representation of a density function, also referred to as the half density, lies in the positive orthant of \mathbb{S}^∞ , making the FR a natural metric for comparing density functions.

5.1.2 Results

\mathbb{T}^2 Results: Figure 2 displays the true (log) density function along with the estimates from each method for a randomly selected experimental replication. Both rows show the same

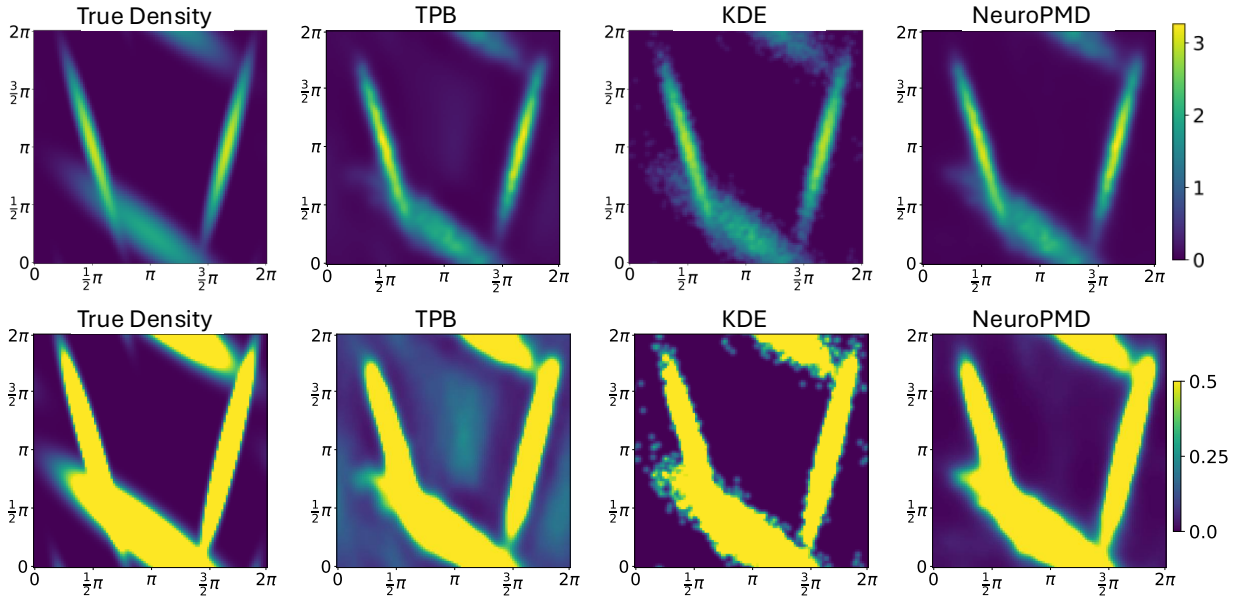


Figure 2: True (log) density function on \mathbb{T}^2 (left column) and estimates of (log) density from each method from a randomly selected experimental replication. Both rows present the same function visualized with different colorbars for enhanced comparison.

functions but with different color scales for better visualization. We observe that the KDE method performs well in capturing the highly peaked mode but struggles with more diffuse modes. This is likely due to the global bandwidth parametrization, which cannot adapt to the spatially varying anisotropy of the underlying density. This can be observed in the relative roughness in the KDE estimate of the most diffuse mode (mixture component at the bottom of the image). TPB accurately recovers the overall structure of the mixture components and captures the smoothness of the more diffuse component better than KDE, as shown in the top row. However, as displayed in the bottom row, TPB tends to overestimate in low-density regions. This tendency is reflected in its comparatively poor performance on the FR metric in Table 1, where the inclusion of the square root amplifies errors in these low-density areas. The issues arises due to the global, finite-rank (band-limited) representation of the Fourier functions. While increasing the marginal frequencies could eventually alleviate this problem, the resulting exponential scaling of the parameter space makes this approach impractical. Compared to the competitors, NeuroPMD offers an effective balance between capturing varying smoothness properties of the function while maintaining low bias in regions of low density. This can be observed quantitatively in Table 1, where

		Method		
		NeuroPMD	KDE	TPB
\mathbb{T}^2	FR	$0.136 \pm (2.08 \times 10^{-3})$	$0.156 \pm (7.65 \times 10^{-4})$	$0.203 \pm (1.43 \times 10^{-3})$
	nISE	$0.0148 \pm (8.17 \times 10^{-4})$	$0.0235 \pm (3.96 \times 10^{-4})$	$0.0165 \pm (5.56 \times 10^{-4})$
\mathbb{T}^4	FR	$0.242 \pm (8.16 \times 10^{-3})$	$1.059 \pm (1.48 \times 10^{-4})$	$0.430 \pm (3.81 \times 10^{-4})$
	nISE	$0.0608 \pm (6.93 \times 10^{-3})$	$0.938 \pm (1.06 \times 10^{-5})$	$0.0764 \pm (3.56 \times 10^{-4})$

Table 1: Monte Carlo average simulation results for density estimation on \mathbb{T}^2 and \mathbb{T}^4 .

The table compares the performance of NeuroPMD, KDE, and TPB using the normalized $L^2(\Omega)$ error (nISE) and Fisher-Rao (FR) metric. Average errors and standard errors (in parentheses) demonstrate that NeuroPMD achieves the best overall performance across both metrics and domains.

NeuroPMD displays the lowest average error in both metrics across replications. Comparing TPB to NeuroPMD, the better performance of the latter can be attributed to its compositional framework. As shown in Theorem 1, the NeuroPMD estimator on \mathbb{T}^D uses a basis of sinusoidal functions whose weights, frequencies, and phase shifts are adaptively learned from the data. In contrast, TPB is restricted to linear weights on a tensor-product expansion over a fixed set of frequencies, limiting its flexibility and adaptability.

\mathbb{T}^4 **Results:** The bottom rows of Table 1 provide a quantitative comparison between the methods in the high-dimensional \mathbb{T}^4 case. The results show that our NeuroPMD method consistently outperforms both the KDE and TPB methods. A notable decline in the performance of KDE is observed when transitioning from the \mathbb{T}^2 to the \mathbb{T}^4 case. This degradation is largely attributable to the CV-based bandwidth selection, which consistently chooses a very small von-Mises concentration (i.e., a large bandwidth), resulting in significantly over-smoothed estimates. Through post-hoc experimentation, we were able to identify some larger concentrations that did lead to lower FR and nISE. Still, none of these configurations achieved the performance levels of NeuroPMD. Identifying the optimal bandwidth for multidimensional density estimation is notoriously challenging. Moreover, even with an optimal global bandwidth, the fits are likely to exhibit local over- and/or under-smoothing

due to spatial variations in the true density’s smoothness and anisotropy. This further underscores the importance of the data-adaptive nature of NeuroPMD: its representation space in \mathbb{T}^D being a large set of data-adaptive Fourier functions (Theorem 1), facilitating adaptation to the localized features of the density. While TPB significantly outperforms KDE, it remains inferior to NeuroPMD, particularly in terms of the FR metric. As observed in the \mathbb{T}^2 case, FR is highly sensitive to bias in low-density regions. The superior performance of NeuroPMD over TPB is particularly notable in this case since TPB actually has more parameters than NeuroPMD, highlighting the parameter efficiency of the compositional structure in (5).

5.2 Real Data Analysis: Brain Connectivity

As outlined in Section 1, a primary motivating application for this work is modeling the spatial distribution of white matter neural fiber connection endpoints on the brain’s cortical surface. These connections, collectively referred to as the *structural connectivity*, can be estimated through a combination of diffusion magnetic resonance imaging (dMRI) (Baliyan et al., 2016) and tractography algorithms (St-Onge et al., 2018). As illustrated in Figure 1 panel A, the inferred tracts map physical connections between different brain regions, effectively reconstructing the complex structural network of the brain. Accurately estimating the density function governing the spatial pattern of connection endpoints is of substantial scientific interest, both for single-subject analysis (Moyer et al., 2017) and as a data representation for population-level studies (Mansour et al., 2022; Consagra et al., 2024a).

5.2.1 Data Description, Implementation Details and Evaluation

In this work, we consider a randomly selected subject from the Adolescent Brain Cognitive Development (ABCD) study (Casey et al., 2018). The structural connectivity endpoint data was inferred from the subject’s diffusion and structural (T1) MRI using the SBCI pipeline (Cole et al., 2021). Briefly, SBCI constructs cortical surfaces using FreeSurfer (Fischl, 2012), where each cortical hemisphere surface is represented using a dense triangular mesh consisting of 163,842 vertices. White matter fiber tracts connecting cortical surface locations are estimated using surface-enhanced tractography (St-Onge et al., 2018).

In total, we observe $n = 242,972$ left-hemisphere to left-hemisphere cortical connections. Each cortical hemisphere surface is approximately homeomorphic to the 2-sphere \mathbb{S}^2 (Fischl et al., 1999). Consequently, connections within a single hemisphere can be parameterized as points on the product space of 2-spheres, such that $(x_1, x_2) \in \mathbb{S}^2 \times \mathbb{S}^2$. Thus, the connectivity can be modeled as a point set on the product space $\Omega = \mathbb{S}^2 \times \mathbb{S}^2$, as shown in Figure 1 panel C, and our goal is to recover the latent density function from the observed intra-hemisphere connectivity.

The eigenfunctions of the LBO on \mathbb{S}^2 are known as the *spherical harmonics*, further details on these functions can be found in Supplemental Section S2.2. We set both maximum marginal *degrees* to be 10 (resulting in 121 harmonic basis for each marginal \mathbb{S}^2), $K = 256$, $L = 6$ hidden layers, and the width of each hidden layer to be 256. We sample the separable tensor product harmonics to form the first layer encoding. We set the batch size $b = n/2$ and $q_1 = q_2 = 10,000$. $T = 10,000$ training iterations are used under the cyclic triangular learning rate policy with minimum and maximum learning rates 10^{-5} and 10^{-3} , respectively. We use the extrinsic form of the Laplacian-based roughness penalty (12) and employ a centered difference scheme to numerically approximate the Hessian in the ambient space \mathbb{R}^6 . Orthogonal basis vectors of the tangent space of $T_{x_d}(\mathbb{S}^2)$ can be calculated analytically (see Section S2.2), and hence the block matrix in proposition 2 can be computed rapidly. The regularization parameter τ is selected using the approach discussed in Section 4.2.

We compare our method with TPB with the same marginal ranks (121^2 basis functions). While specifying a product kernel on Ω is straightforward, the KDE method proves highly impractical in this setting. The difficulty arises not only from the large data size n , but more critically from the extremely high-resolution surface meshes ($> 160,000$ vertices for each marginal \mathbb{S}^2) on which we wish to infer the density function. Therefore, we exclude the KDE method from our comparisons.

Due to the absence of a ground truth density function, we evaluate the estimation performance qualitatively. Specifically, we focus on an anatomically defined region of interest (ROI) on the brain surface and analyze the associated connectivity patterns using

the concept of *marginal connectivity*:

$$\tilde{f}_E(x_2) = \int_{x_1 \in E} \tilde{f}(x_1, x_2) dx_1,$$

where E is a predefined brain ROI, and the integral is approximated numerically using the high-resolution spherical mesh. This evaluation approach enables us to examine the estimated connectivity function through marginal profiles, which are functions on \mathbb{S}^2 and are more amenable to visualization and interpretation. For this study, we focus on the medial orbitofrontal cortex (MOFC) ROI, displayed in red in the top row of Figure 4. The MOFC is an important brain region involved in high-order cognitive processing, and its connectivity is impacted in psychiatric diseases, including depression (Rolls et al., 2020).

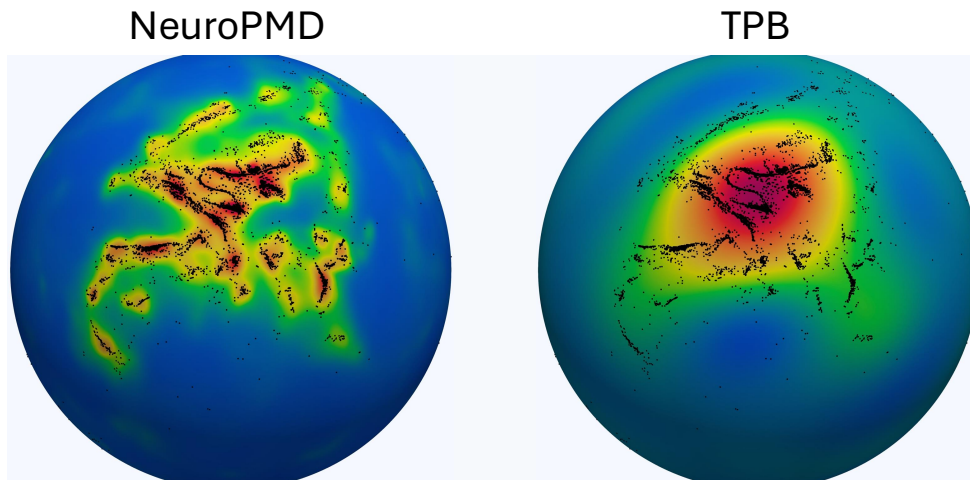


Figure 3: Marginal density function estimates for connections from the medial orbitofrontal cortex (MOFC), generated using our method (left) and tensor product basis (right). Black dots represent the endpoints connected to the MOFC. Color scales are normalized within each image to emphasize differences in the shape of the functions.

5.2.2 Results

Figure 3 shows the marginal density functions \tilde{f}_E for $E = \text{MOFC}$ for both NeuroPMD and TPB. The black points in Figure 3 are endpoints of fiber curves whose other endpoints are located in the MOFC. Comparing the connection point pattern to the estimated \tilde{f}_E , we observe that our method successfully detects nearly all marginal modes and effectively adapts to the data’s highly anisotropic shape. In contrast, the TPB method significantly over-smooths the data, failing to capture the multi-modal and high-frequency structure.

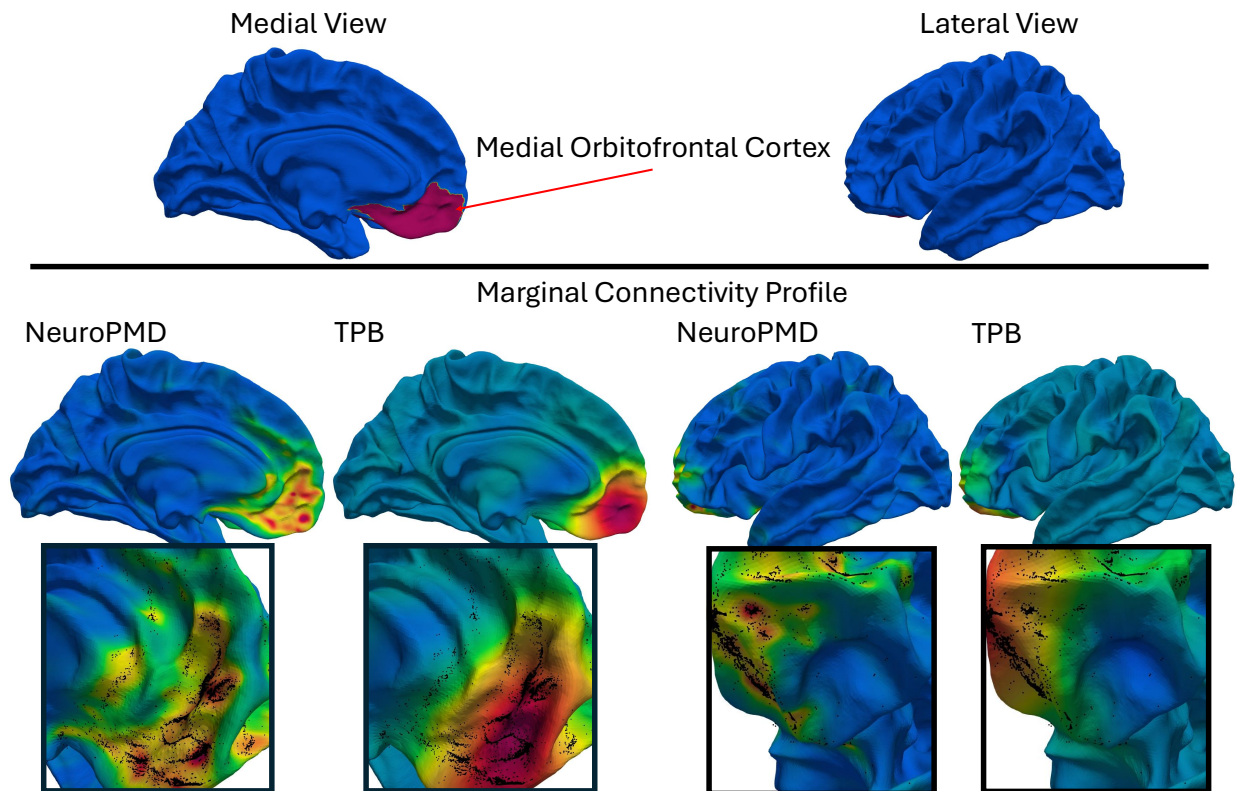


Figure 4: Same as Figure 3, with marginal density functions mapped to the cortical surface. **Top Row:** The MOFC is highlighted in red in both medial (left) and lateral (right) views. **Middle Row:** Comparing the estimated marginal density functions by the NeuroPMD and TPB method. **Bottom Row:** Close-up views of the marginal density functions mapped to the cortical surface. Endpoints of fiber curves connecting to the MOFC are marked in black.

To facilitate biological interpretation, we mapped the marginal density function and connection points back to the cortical surface in Figure 4. The middle and bottom two rows again demonstrate NeuroPMD’s ability to capture the fine details of the connection patterns. In comparison, the TPB estimates appear significantly over-smoothed. The MOFC region is generally known to have strong connections with the anterior cingulate gyrus, pregenual cingulate cortex, frontal pole, and lateral orbitofrontal cortex (Beckmann et al., 2009; Heather Hsu et al., 2020). All of these expected connection patterns are clearly reflected in the marginal density estimates of NeuroPMD. Additionally, studies suggest complex connectivity patterns within the MOFC (Chapter 3; Zald and Rauch (2006)). The detailed connectivity within the MOFC is evident in the zoomed-in region on the left, showing a distinct multi-modal and anisotropic spatial structure.

Supplemental Figures S5 and S6 in Section S5.2 highlight the variability in intra- and inter-MOFC connection patterns across several ABCD subjects by showing their marginal density functions estimated by NeuroPMD. It is notable that the within MOFC structure is entirely lost when using traditional ROI-based network representations, where between-ROI connections are reduced to a single summary statistic (e.g., a count), and within-ROI connections are ignored (Chung et al., 2021). We speculate that integrating the proposed deep neural field model as a data representation could enhance the power of downstream neuroscientific tasks, such as cognitive trait and neuropsychiatric disease prediction, compared to traditional ROI-based models. However, determining the optimal approach for such integration is an open question for future work.

6 Conclusion

This work introduces a novel deep neural network methodology for density function estimation on product Riemannian manifolds. By carefully designing the network architecture and stochastic gradient estimation, our method avoids the curse of dimensionality that afflicts traditional approaches to flexible density estimation in high-dimensional settings. To promote convergence and properly regularize our estimates, a roughness penalty based on the Laplace-Beltrami operator is incorporated. To our knowledge, this is the first approach to use a deep neural network for flexible density estimation on product manifold domains. Simulation studies demonstrate improved performance over traditional approaches, particularly in high-dimensional domains, and a real-world application to a challenging neuroscience dataset shows its practical utility in revealing detailed neural connectivity patterns on the brain’s surface.

Code: Code implementing our model and algorithms has been made publicly available: <https://github.com/Will-Consagra/NeuroPMD>.

References

Arnone, E., Ferraccioli, F., Pigolotti, C., and Sangalli, L. M. (2022). A roughness penalty approach to estimate densities over two-dimensional manifolds. *Computational Statistics & Data Analysis*, 174:107527.

- Baliyan, V., Das, C. J., Sharma, R., and Gupta, A. K. (2016). Diffusion weighted imaging: technique and applications. *World journal of radiology*, 8(9):785.
- Bates, J. and Mio, W. (2014). Density estimators of gaussian type on closed riemannian manifolds. *Journal of Mathematical Imaging and Vision*, 50(1):53–59.
- Baydin, A. G., Pearlmutter, B. A., Radul, A. A., and Siskind, J. M. (2018). Automatic differentiation in machine learning: a survey. *Journal of Machine Learning Research*, 18(153):1–43.
- Beckmann, M., Johansen-Berg, H., and Rushworth, M. F. S. (2009). Connectivity-based parcellation of human cingulate cortex and its relation to functional specialization. *Journal of Neuroscience*, 29(4):1175–1190.
- Begu, B., Panzeri, S., Arnone, E., Carey, M., and Sangalli, L. M. (2024). A nonparametric penalized likelihood approach to density estimation of space–time point patterns. *Spatial Statistics*, 61:100824.
- Bentley, J. L. (1975). Multidimensional binary search trees used for associative searching. *Commun. ACM*, 18(9):509–517.
- Berry, T. and Sauer, T. (2017). Density estimation on manifolds with boundary. *Computational Statistics & Data Analysis*, 107:1–17.
- Bottou, L., Curtis, F. E., and Nocedal, J. (2018). Optimization methods for large-scale machine learning. *SIAM Review*, 60(2):223–311.
- Canzani, Y. (2013). Analysis on manifolds via the laplacian. Harvard University.
- Cao, Y., Fang, Z., Wu, Y., Zhou, D.-X., and Gu, Q. (2019). Towards understanding the spectral bias of deep learning. In *International Joint Conference on Artificial Intelligence*.
- Casey, B. et al. (2018). The adolescent brain cognitive development (abcd) study: Imaging acquisition across 21 sites. *Developmental Cognitive Neuroscience*, 32:43–54. The Adolescent Brain Cognitive Development (ABCD) Consortium: Rationale, Aims, and Assessment Strategy.

- Chen, L.-H. and Jiang, C.-R. (2017). Multi-dimensional functional principal component analysis. *Statistics and Computing*, 27(5):1181–1192.
- Chung, J., Bridgeford, E., Arroyo, J., Pedigo, B. D., Saad-Eldin, A., Gopalakrishnan, V., Xiang, L., Priebe, C. E., and Vogelstein, J. T. (2021). Statistical connectomics. *Annual Review of Statistics and Its Application*, 8(Volume 8, 2021):463–492.
- Cleanthous, G., Georgiadis, A. G., Kerkycharian, G., Petrushev, P., and Picard, D. (2020). Kernel and wavelet density estimators on manifolds and more general metric spaces. *Bernoulli*, 26(3):1832 – 1862.
- Cole, M., Murray, K., St-Onge, E., Risk, B., Zhong, J., Schifitto, G., Descoteaux, M., and Zhang, Z. (2021). Surface-based connectivity integration: An atlas-free approach to jointly study functional and structural connectivity. *Human Brain Mapping*, 42(11):3481–3499.
- Consagra, W., Cole, M., Qiu, X., and Zhang, Z. (2024a). Continuous and atlas-free analysis of brain structural connectivity. *Annals of Applied Statistics*.
- Consagra, W., Venkataraman, A., and Qiu, X. (2024b). Efficient multidimensional functional data analysis using marginal product basis systems. *Journal of Computational and Graphical Statistics*, 33(2):567–577.
- Dupont, E., Kim, H., Eslami, S. M. A., Rezende, D. J., and Rosenbaum, D. (2022). From data to functa: Your data point is a function and you can treat it like one. In Chaudhuri, K., Jegelka, S., Song, L., Szepesvari, C., Niu, G., and Sabato, S., editors, *Proceedings of the 39th International Conference on Machine Learning*, volume 162 of *Proceedings of Machine Learning Research*, pages 5694–5725. PMLR.
- Eldan, R. and Shamir, O. (2016). The power of depth for feedforward neural networks. In Feldman, V., Rakhlin, A., and Shamir, O., editors, *29th Annual Conference on Learning Theory*, volume 49 of *Proceedings of Machine Learning Research*, pages 907–940, Columbia University, New York, New York, USA. PMLR.
- Faroughi, S. A., Soltanmohammadi, R., Datta, P., Mahjour, S. K., and Faroughi, S. (2024).

- Physics-informed neural networks with periodic activation functions for solute transport in heterogeneous porous media. *Mathematics*, 12(1).
- Fathony, R., Sahu, A. K., Willmott, D., and Kolter, J. Z. (2021). Multiplicative filter networks. In *International Conference on Learning Representations*.
- Ferraccioli, F., Arnone, E., Finos, L., Ramsay, J. O., and Sangalli, L. M. (2021). Nonparametric Density Estimation Over Complicated Domains. *Journal of the Royal Statistical Society Series B: Statistical Methodology*, 83(2):346–368.
- Fischl, B. (2012). Freesurfer. *NeuroImage*, 62(2):774–781. 20 YEARS OF fMRI.
- Fischl, B., Sereno, M. I., and Dale, A. M. (1999). Cortical surface-based analysis: I: Inflation, flattening, and a surface-based coordinate system. *NeuroImage*, 9(2):195–207.
- Ghadimi, S. and Lan, G. (2013). Stochastic first- and zeroth-order methods for nonconvex stochastic programming. *SIAM Journal on Optimization*, 23(4):2341–2368.
- Good, I. J. and Gaskins, R. A. (1971). Nonparametric roughness penalties for probability densities. *Biometrika*, 58(2):255–277.
- Hall, P. and Marron, J. S. (1987). Extent to which least-squares cross-validation minimises integrated square error in nonparametric density estimation. *Probability Theory and Related Fields*, 74(4):567–581.
- Harlim, J., Jiang, S. W., and Peoples, J. W. (2023). Radial basis approximation of tensor fields on manifolds: From operator estimation to manifold learning. *Journal of Machine Learning Research*, 24(345):1–85.
- Heather Hsu, C.-C., Rolls, E. T., Huang, C.-C., Chong, S. T., Zac Lo, C.-Y., Feng, J., and Lin, C.-P. (2020). Connections of the Human Orbitofrontal Cortex and Inferior Frontal Gyrus. *Cerebral Cortex*, 30(11):5830–5843.
- Hornik, K., Stinchcombe, M., and White, H. (1989). Multilayer feedforward networks are universal approximators. *Neural Networks*, 2(5):359–366.

- Karppa, M., Aumüller, M., and Pagh, R. (2022). Deann: Speeding up kernel-density estimation using approximate nearest neighbor search. In Camps-Valls, G., Ruiz, F. J. R., and Valera, I., editors, *Proceedings of The 25th International Conference on Artificial Intelligence and Statistics*, volume 151 of *Proceedings of Machine Learning Research*, pages 3108–3137. PMLR.
- Kim, Y. T. and Park, H. S. (2013). Geometric structures arising from kernel density estimation on riemannian manifolds. *Journal of Multivariate Analysis*, 114:112–126.
- Kingma, D. and Ba, J. (2015). Adam: A method for stochastic optimization. In *International Conference on Learning Representations (ICLR)*, San Diego, CA, USA.
- Krizhevsky, A., Sutskever, I., and Hinton, G. E. (2012). Imagenet classification with deep convolutional neural networks. In Pereira, F., Burges, C., Bottou, L., and Weinberger, K., editors, *Advances in Neural Information Processing Systems*, volume 25. Curran Associates, Inc.
- Kurz, G., Gilitschenski, I., Pfaff, F., Drude, L., Hanebeck, U. D., Haeb-Umbach, R., and Siegwart, R. Y. (2019). Directional statistics and filtering using libDirectional. *Journal of Statistical Software*, 89(4):1–31.
- Lapedes, A. and Farber, R. (1987). Nonlinear signal processing using neural networks: Prediction and system modelling.
- Mansour, S., Seguin, C., Smith, R. E., and Zalesky, A. (2022). Connectome spatial smoothing (css): Concepts, methods, and evaluation. *NeuroImage*, 250:118930.
- Mardia, K. and Jupp, P. (2009). *Directional Statistics*. Wiley Series in Probability and Statistics. Wiley.
- Mei, H. and Eisner, J. M. (2017). The neural hawkes process: A neurally self-modulating multivariate point process. In Guyon, I., Luxburg, U. V., Bengio, S., Wallach, H., Fergus, R., Vishwanathan, S., and Garnett, R., editors, *Advances in Neural Information Processing Systems*, volume 30. Curran Associates, Inc.

- Moyer, D., Gutman, B. A., Faskowitz, J., Jahanshad, N., and Thompson, P. M. (2017). Continuous representations of brain connectivity using spatial point processes. *Medical Image Analysis*, 41:32 – 39.
- Owen, A. B. (1998). Scrambling sobol’ and niederreiter–xing points. *Journal of Complexity*, 14(4):466–489.
- Parascandolo, G., Huttunen, H., and Virtanen, T. (2017). Taming the waves: sine as activation function in deep neural networks.
- Pavlos Zouboulouglou, E. G.-P. and Marron, J. S. (2023). Scaled torus principal component analysis. *Journal of Computational and Graphical Statistics*, 32(3):1024–1035.
- Pelletier, B. (2005). Kernel density estimation on riemannian manifolds. *Statistics & Probability Letters*, 73(3):297–304.
- Rahaman, N., Baratin, A., Arpit, D., Draxler, F., Lin, M., Hamprecht, F., Bengio, Y., and Courville, A. (2019). On the spectral bias of neural networks. In Chaudhuri, K. and Salakhutdinov, R., editors, *Proceedings of the 36th International Conference on Machine Learning*, volume 97 of *Proceedings of Machine Learning Research*, pages 5301–5310. PMLR.
- Rahimi, A. and Recht, B. (2007). Random features for large-scale kernel machines. In Platt, J., Koller, D., Singer, Y., and Roweis, S., editors, *Advances in Neural Information Processing Systems*, volume 20. Curran Associates, Inc.
- Raissi, M., Perdikaris, P., and Karniadakis, G. (2019). Physics-informed neural networks: A deep learning framework for solving forward and inverse problems involving nonlinear partial differential equations. *Journal of Computational Physics*, 378:686–707.
- Reuter, M., Biasotti, S., Giorgi, D., Patanè, G., and Spagnuolo, M. (2009). Discrete laplace–beltrami operators for shape analysis and segmentation. *Computers & Graphics*, 33(3):381–390. IEEE International Conference on Shape Modelling and Applications 2009.

- Rolls, E. T., Cheng, W., and Feng, J. (2020). The orbitofrontal cortex: reward, emotion and depression. *Brain Communications*, 2(2):fcaa196.
- Silverman, B. W. (1982). On the Estimation of a Probability Density Function by the Maximum Penalized Likelihood Method. *The Annals of Statistics*, 10(3):795 – 810.
- Simpson, D., Illian, J. B., Lindgren, F., Sørbye, S. H., and Rue, H. (2016). Going off grid: computationally efficient inference for log-Gaussian Cox processes. *Biometrika*, 103(1):49–70.
- Sitzmann, V., Martel, J. N. P., Bergman, A. W., Lindell, D. B., and Wetzstein, G. (2020). Implicit neural representations with periodic activation functions. In *Proceedings of the 34th International Conference on Neural Information Processing Systems*, NIPS’20, Red Hook, NY, USA. Curran Associates Inc.
- Smith, L. N. (2017). Cyclical learning rates for training neural networks. In *2017 IEEE Winter Conference on Applications of Computer Vision (WACV)*, pages 464–472.
- Snoek, J., Larochelle, H., and Adams, R. P. (2012). Practical bayesian optimization of machine learning algorithms. In Pereira, F., Burges, C., Bottou, L., and Weinberger, K., editors, *Advances in Neural Information Processing Systems*, volume 25. Curran Associates, Inc.
- St-Onge, E., Daducci, A., Girard, G., and Descoteaux, M. (2018). Surface-enhanced tractography (set). *NeuroImage*, 169:524–539.
- Takikawa, T., Litalien, J., Yin, K., Kreis, K., Loop, C., Nowrouzezahrai, D., Jacobson, A., McGuire, M., and Fidler, S. (2021). Neural geometric level of detail: Real-time rendering with implicit 3D shapes. In *Proceedings of the IEEE/CVF Conference on Computer Vision and Pattern Recognition (CVPR)*.
- Tancik, M., Srinivasan, P., Mildenhall, B., Fridovich-Keil, S., Raghavan, N., Singhal, U., Ramamoorthi, R., Barron, J., and Ng, R. (2020). Fourier features let networks learn high frequency functions in low dimensional domains. In Larochelle, H., Ranzato, M., Hadsell, R., Balcan, M., and Lin, H., editors, *Advances in Neural Information Processing Systems*, volume 33, pages 7537–7547. Curran Associates, Inc.

- Telgarsky, M. (2015). Representation benefits of deep feedforward networks. *arXiv: cs.LG*.
- Tsuchida, R., Ong, C. S., and Sejdinovic, D. (2023). Squared neural families: A new class of tractable density models. In Oh, A., Naumann, T., Globerson, A., Saenko, K., Hardt, M., and Levine, S., editors, *Advances in Neural Information Processing Systems*, volume 36, pages 73943–73968. Curran Associates, Inc.
- Tsuchida, R., Ong, C. S., and Sejdinovic, D. (2024). Exact, fast and expressive poisson point processes via squared neural families. In *AAAI*.
- Wang, J., Wong, R. K. W., and Zhang, X. (2020). Low-rank covariance function estimation for multidimensional functional data. *Journal of the American Statistical Association*, 0(0):1–14.
- Wang, S. and Cao, G. (2022). Robust deep neural network estimation for multi-dimensional functional data. *Electronic Journal of Statistics*, 16(2):6461 – 6488.
- Wang, Z. and Scott, D. W. (2019). Nonparametric density estimation for high-dimensional data—algorithms and applications. *WIREs Computational Statistics*, 11(4):e1461.
- Ward, S., Battey, H. S., and Cohen, E. A. K. (2023). Nonparametric estimation of the intensity function of a spatial point process on a Riemannian manifold. *Biometrika*.
- Xiao, S., Farajtabar, M., Ye, X., Yan, J., Song, L., and Zha, H. (2017). Wasserstein learning of deep generative point process models. In Guyon, I., Luxburg, U. V., Bengio, S., Wallach, H., Fergus, R., Vishwanathan, S., and Garnett, R., editors, *Advances in Neural Information Processing Systems*, volume 30. Curran Associates, Inc.
- Xie, Y., Takikawa, T., Saito, S., Litany, O., Yan, S., Khan, N., Tombari, F., Tompkin, J., Sitzmann, V., and Sridhar, S. (2022). Neural fields in visual computing and beyond. *Computer Graphics Forum*, 41(2):641–676.
- Yu, T. and Zhu, H. (2020). Hyper-parameter optimization: A review of algorithms and applications. *arXiv: cs.LG*, abs/2003.05689.
- Yüce, G., Ortiz-Jiménez, G., Besbinar, B., and Frossard, P. (2022). A structured dictionary perspective on implicit neural representations.

Zald, D. and Rauch, S. (2006). *The Orbitofrontal Cortex*. Oxford University Press.

Zhou, Z. and Yu, R. (2023). Automatic integration for spatiotemporal neural point processes. In Oh, A., Naumann, T., Globerson, A., Saenko, K., Hardt, M., and Levine, S., editors, *Advances in Neural Information Processing Systems*, volume 36, pages 50237–50253. Curran Associates, Inc.

SUPPLEMENTAL MATERIAL

S1 Proofs

S1.1 Proposition 1

Proof. Note that

$$\begin{aligned}
 \mathbb{E}[\mathbf{a}^b(\boldsymbol{\theta})] &= \frac{1}{b} \sum_{i=1}^b \mathbb{E} \left[\frac{\partial}{\partial \boldsymbol{\theta}} v_{\boldsymbol{\theta}}(x_{1i}, \dots, x_{Di}) \right] = \frac{1}{b} \sum_{i=1}^b \mathbb{E} \left[\sum_{j=1}^n \mathbb{I}\{i = j\} \frac{\partial}{\partial \boldsymbol{\theta}} v_{\boldsymbol{\theta}}(x_{1j}, \dots, x_{Dj}) \right] \\
 &= \frac{1}{b} \sum_{i=1}^b \sum_{j=1}^n p(i = j) \frac{\partial}{\partial \boldsymbol{\theta}} v_{\boldsymbol{\theta}}(x_{1j}, \dots, x_{Dj}) = \frac{1}{b} \sum_{i=1}^b \frac{1}{n} \sum_{j=1}^n \frac{\partial}{\partial \boldsymbol{\theta}} v_{\boldsymbol{\theta}}(x_{1j}, \dots, x_{Dj}) \\
 &= \frac{1}{n} \sum_{j=1}^n \frac{\partial}{\partial \boldsymbol{\theta}} v_{\boldsymbol{\theta}}(x_{1j}, \dots, x_{Dj}),
 \end{aligned}$$

where the expectation is being taken with respect to the uniform distribution over the indices $\{1, \dots, n\}$. Now, considering the latter two terms of the sum, $\mathbf{b}^{q_1}(\boldsymbol{\theta})$ and $\mathbf{c}_{\tau}^{q_2}(\boldsymbol{\theta})$, and taking the expectation with respect to the uniform measure on Ω , we have

$$\begin{aligned}
 \mathbb{E}[\mathbf{b}^{q_1}(\boldsymbol{\theta})] &= \mathbb{E} \left[\frac{\text{Vol}(\Omega)}{q_1} \sum_{j=1}^{q_1} \frac{\partial}{\partial \boldsymbol{\theta}} \exp(v_{\boldsymbol{\theta}}(x_{1j}, \dots, x_{Dj})) \right] \\
 &= \frac{\text{Vol}(\Omega)}{q_1} \sum_{j=1}^{q_1} \mathbb{E} \left[\frac{\partial}{\partial \boldsymbol{\theta}} \exp(v_{\boldsymbol{\theta}}(x_{1j}, \dots, x_{Dj})) \right] \\
 &= \frac{\text{Vol}(\Omega)}{q_1} \sum_{j=1}^{q_1} \frac{1}{\text{Vol}(\Omega)} \int_{\Omega} \frac{\partial}{\partial \boldsymbol{\theta}} \exp(v_{\boldsymbol{\theta}}(x_1, \dots, x_D)) d\omega \\
 &= \int_{\Omega} \frac{\partial}{\partial \boldsymbol{\theta}} \exp(v_{\boldsymbol{\theta}}(x_1, \dots, x_D)) d\omega,
 \end{aligned}$$

and thus similarly

$$\mathbb{E}[\mathbf{c}_{\tau}^{q_2}(\boldsymbol{\theta})] = \tau \int_{\Omega} \frac{\partial}{\partial \boldsymbol{\theta}} [\Delta_{\Omega} v_{\boldsymbol{\theta}}]^2 d\omega.$$

Hence,

$$\begin{aligned}
 \mathbb{E}[\mathbf{a}^b(\boldsymbol{\theta}) - \mathbf{b}^{q_1}(\boldsymbol{\theta}) - \mathbf{c}_{\tau}^{q_2}(\boldsymbol{\theta})] &= \frac{1}{n} \sum_{j=1}^n \frac{\partial}{\partial \boldsymbol{\theta}} v_{\boldsymbol{\theta}}(x_{1j}, \dots, x_{Dj}) - \int_{\Omega} \frac{\partial}{\partial \boldsymbol{\theta}} \exp(v_{\boldsymbol{\theta}}) d\omega - \tau \int_{\Omega} \frac{\partial}{\partial \boldsymbol{\theta}} [\Delta_{\Omega} v_{\boldsymbol{\theta}}]^2 d\omega \\
 &= \frac{\partial}{\partial \boldsymbol{\theta}} \mathcal{L}(o, \boldsymbol{\theta}),
 \end{aligned}$$

as desired. □

S1.2 Proposition 2

For convenience, we begin with notation and preliminaries. Let $\mathcal{M} \subset \mathbb{R}^m$ be a p -dimensional closed manifold embedded in ambient space \mathbb{R}^m . Following the formulation in Harlim et al. (2023), we approximate the point-wise application of differential operators on smooth function $v : \mathcal{M} \mapsto \mathbb{R}$ by first calculating a differential operator in the ambient space \mathbb{R}^m , followed by a projection onto the local tangent space $T_x(\mathcal{M})$ of the manifold. This allows us to leverage the automatic differentiation of the estimator (5) or simple discrete differential operator approximations in the ambient space followed by a projection to approximate the operators of interest. For any $x \in \mathcal{M}$, denote the homeomorphic local parameterization $l : O \subset \mathbb{R}^p \mapsto V \cap \mathcal{M} \subset \mathbb{R}^m$, for open sets O, V . Let $\gamma = l^{-1}(x)$, then a basis for $T_x(\mathcal{M})$ is defined by $\{\frac{\partial l}{\partial \gamma_i}(\gamma)\}_{i=1}^p$. Denote the matrix $\mathbf{A}_l(x) \in \mathbb{R}^{m \times p}$, whose columns are given by the vectors $\frac{\partial l}{\partial \gamma_i}(\gamma)$. Define the projection matrix

$$\mathbf{P} := \mathbf{P}(x) = \mathbf{A}_l(x)(\mathbf{A}_l^\top(x)\mathbf{A}_l(x))^{-1}\mathbf{A}_l^\top(x),$$

where from here on the dependence on x is assumed and dropped for clarity. Let $\{t_i\}_{i=1}^p$ be a set of orthogonal vectors in \mathbb{R}^m that span $T_x(\mathcal{M})$ and denote $\mathbf{T} = [t_1, \dots, t_p] \in \mathbb{R}^{m \times p}$. From proposition 2.1 in Harlim et al. (2023), we have that $\mathbf{P} = \mathbf{T}\mathbf{T}^\top$ and the manifold gradient can be written as

$$\nabla_{\mathcal{M}}v(x) = \mathbf{P}\nabla_{\mathbb{R}^m}v(x). \tag{S.1}$$

Using this definition of the gradient, the Laplace-Beltrami operator has the following formulation in ambient space coordinates

$$\Delta_{\mathcal{M}}v(x) = \text{div}_{\mathcal{M}}\nabla_{\mathcal{M}}v(x) = (\mathbf{P}\nabla_{\mathbb{R}^m}) \cdot (\mathbf{P}\nabla_{\mathbb{R}^m})v(x), \tag{S.2}$$

where $\nabla_{\mathbb{R}^m}$ denotes the standard Euclidean gradient in \mathbb{R}^m . Given these preliminaries, we provide the proof to Proposition 2.

Proof. From (S.1), we can write the gradient as

$$\nabla_{\mathcal{M}}v(x) = \mathbf{P}\nabla_{\mathbb{R}^m}v(x) = \begin{pmatrix} \sum_{i=1}^m \mathbf{P}_{1i}\partial_i v(x) \\ \vdots \\ \sum_{i=1}^m \mathbf{P}_{mi}\partial_i v(x). \end{pmatrix}$$

Clearly, this produces a vector field on the manifold. Denote $\mathbf{P}_{i,\cdot} \in \mathbb{R}^m$ as the row vector corresponding to the i 'th row of \mathbf{P} , and denote $\mathbf{H}_{\mathbb{R}^m}(v)(x) \in \mathbb{R}^{m \times m}$ to be the standard Euclidean Hessian matrix of v at x , with l, i element $\partial_{li}v(x)$. Then the manifold divergence can be written as

$$\begin{aligned}
\operatorname{div}_{\mathcal{M}} \nabla_{\mathcal{M}} v(x) &= \mathbf{P} \nabla_{\mathbb{R}^m} \cdot \nabla_{\mathcal{M}} v(x) = \mathbf{P} \nabla_{\mathbb{R}^m} \cdot \begin{pmatrix} \sum_{i=1}^m \mathbf{P}_{1i} \partial_i v(x) \\ \vdots \\ \sum_{i=1}^m \mathbf{P}_{mi} \partial_i v(x) \end{pmatrix} \\
&= \operatorname{sum} \left(\begin{pmatrix} \mathbf{P}_{11} \partial_1 (\sum_{i=1}^m \mathbf{P}_{1i} \partial_i v(x)) + \dots + \mathbf{P}_{1m} \partial_m (\sum_{i=1}^m \mathbf{P}_{1i} \partial_i v(x)) \\ \vdots \\ \mathbf{P}_{m1} \partial_1 (\sum_{i=1}^m \mathbf{P}_{mi} \partial_i v(x)) + \dots + \mathbf{P}_{mm} \partial_m (\sum_{i=1}^m \mathbf{P}_{mi} \partial_i v(x)) \end{pmatrix} \right) \\
&= \operatorname{sum} \left(\begin{pmatrix} (\sum_{i=1}^m \mathbf{P}_{11} \mathbf{P}_{1i} \partial_1 \partial_i v(x)) + \dots + (\sum_{i=1}^m \mathbf{P}_{1m} \mathbf{P}_{1i} \partial_m \partial_i v(x)) \\ \vdots \\ (\sum_{i=1}^m \mathbf{P}_{m1} \mathbf{P}_{mi} \partial_1 \partial_i v(x)) + \dots + (\sum_{i=1}^m \mathbf{P}_{mm} \mathbf{P}_{mi} \partial_m \partial_i v(x)) \end{pmatrix} \right) \\
&= \operatorname{sum} \left(\begin{pmatrix} \sum_{l=1}^m \sum_{i=1}^m \mathbf{P}_{1l} \mathbf{P}_{1i} \partial_l \partial_i v(x) \\ \vdots \\ \sum_{l=1}^m \sum_{i=1}^m \mathbf{P}_{ml} \mathbf{P}_{mi} \partial_l \partial_i v(x) \end{pmatrix} \right) = \operatorname{sum} \left(\begin{pmatrix} \sum_{l=1}^m \sum_{i=1}^m \mathbf{P}_{1l} \mathbf{P}_{1i} \partial_{li} v(x) \\ \vdots \\ \sum_{l=1}^m \sum_{i=1}^m \mathbf{P}_{ml} \mathbf{P}_{mi} \partial_{li} v(x) \end{pmatrix} \right) \\
&= \operatorname{sum} \left(\begin{pmatrix} \mathbf{P}_{1,\cdot} \mathbf{H}_{\mathbb{R}^m}(v)(x) \mathbf{P}_{1,\cdot}^\top \\ \vdots \\ \mathbf{P}_{m,\cdot} \mathbf{H}_{\mathbb{R}^m}(v)(x) \mathbf{P}_{m,\cdot}^\top \end{pmatrix} \right) = \sum_{i=1}^m \mathbf{P}_{i,\cdot} \mathbf{H}_{\mathbb{R}^m}(v)(x) \mathbf{P}_{i,\cdot}^\top,
\end{aligned}$$

where $\operatorname{sum}()$ is the sum operator on the vector. Hence, the Laplace-Beltrami operator is given as:

$$\Delta_{\mathcal{M}}[v](x) = \operatorname{div}_{\mathcal{M}} \nabla_{\mathcal{M}}[v](x) = \sum_{i=1}^m \mathbf{P}_{i,\cdot} \mathbf{H}_{\mathbb{R}^m}(v)(x) \mathbf{P}_{i,\cdot}^\top. \quad (\text{S.3})$$

With slight abuse of notation, we now define $v : \Omega \mapsto \mathbb{R}$. For a product manifold $\Omega = \times_{d=1}^D \mathcal{M}_d$, where $\mathcal{M}_d \subset \mathbb{R}^{m_d}$ are p_d dimension smooth manifolds, recall that the Laplace-Beltrami operator is given by $\Delta_{\Omega} = \sum_{d=1}^D \Delta_{\mathcal{M}_d}$ (Canzani, 2013). Denote the block matrix

$$\mathbf{P} = \operatorname{BlockDiag} \left(\mathbf{P}^{(1)}, \dots, \mathbf{P}^{(D)} \right) = \begin{pmatrix} \mathbf{P}^{(1)} & 0 & \dots & 0 \\ 0 & \mathbf{P}^{(2)} & \dots & 0 \\ \vdots & \vdots & \ddots & \vdots \\ 0 & 0 & \dots & \mathbf{P}^{(D)} \end{pmatrix},$$

where $\mathbf{P}^{(d)}$ is the projection matrix for the marginal manifold \mathcal{M}_d . Combining this with definition (S.3), denoting $M = \sum_{d=1}^D m_d$, the final result follows directly as

$$\Delta_{\Omega}[v] = \sum_{d=1}^D \Delta_{\mathcal{M}_d}[v] = \sum_{d=1}^D \sum_{i_d=1}^{m_d} \mathbf{P}_{i_d}^{(d)} \mathbf{H}_{\mathbb{R}^{m_d}}(v) [\mathbf{P}_{i_d}^{(d)}]^{\top} = \sum_{i=1}^M \mathbf{P}_i \mathbf{H}_{\mathbb{R}^M}[v] \mathbf{P}_i^{\top}.$$

□

S1.3 Proof of Theorem 1

In the following lemma, we prove that tensor product basis $\psi_k(\mathbf{x})$ can be written as the sum of Fourier mappings that take the whole \mathbf{x} vector as input.

Lemma S1. Denote $p_D(\mathbf{x}) = \prod_{d=1}^D \cos(w_d x_d + a_d)$, with $D \in \mathbb{Z}^+$ and $w_d \in \mathbb{Z}^+, d = 1, \dots, D$, then

$$p_D(\mathbf{x}) = \frac{1}{|\mathcal{W}_D|} \sum_{\mathbf{w}_{\ell} \in \mathcal{W}_D} \cos(\langle \mathbf{w}_{\ell}, \mathbf{x} \rangle + b_{\ell}), b_{\ell} \in \mathbb{R}, \quad (\text{S.4})$$

where $\mathcal{W}_D = \{(w_1, c_{\ell 2} w_2, \dots, c_{\ell D} w_D) : c_{\ell d} \in \{-1, 1\} \text{ for } d = 2, \dots, D\}$ is a set of frequencies; $1 \leq \ell \leq 2^{D-1}$ is the index for the frequency vector in \mathcal{W}_D and \mathbf{w}_{ℓ} denotes the ℓ -th frequency vector; $b_{\ell} = a_1 + \sum_{d=2}^D c_{\ell d} a_d$ is the corresponding phase to \mathbf{w}_{ℓ} ; and $|\mathcal{W}_D| = 2^{D-1}$ is the cardinality of \mathcal{W}_D .

Proof of Lemma S1. The lemma can be proved by induction along with $\cos a \cos b = (\cos(a+b) + \cos(a-b))/2$.

Base case. When $D = 1$, $p_1(x) = \cos(w_1 x + a_1)$. Therefore, the corresponding set of frequencies $\mathcal{W}_1 = \{(w_1)\}$. When $D = 2$, $p_2(\mathbf{x}) = \{\cos(w_1 x_1 + w_2 x_2 + a_1 + a_2) + \cos(w_1 x_1 - w_2 x_2 + a_1 - a_2)\}/2$, indicating $\mathcal{W}_2 = \{(w_1, w_2), (w_1, -w_2)\}$, and $b_{\ell} = a_1 + c_{\ell 2} a_2$ where $c_{\ell 2} = 1$ if $\mathbf{w}_{\ell} = (w_1, w_2)$, and $c_{\ell 2} = -1$ if $\mathbf{w}_{\ell} = (w_1, -w_2)$.

Inductive step. For clarity, we write $\mathbf{w}_{\ell, D} \equiv \mathbf{w}_{\ell}$ to be the elements of \mathcal{W}_D and denote $\mathbf{x}_{1:D} \in \mathbb{T}^D$ to be the vector consisting of the first D elements of $\mathbf{x} \in \mathbb{T}^{D+1}$. Suppose (S.4)

holds for some D and $D \geq 2$, we derive the form of $p_{D+1}(\mathbf{x})$ from $p_D(\mathbf{x}_{1:D})$ as follows.

$$\begin{aligned}
p_{D+1}(\mathbf{x}) &= p_D(\mathbf{x}_{1:D}) \cdot \cos(w_{D+1}x_{D+1} + a_{D+1}) \\
&= 2^{-D+1} \sum_{\ell=1}^{2^{D-1}} \cos(\langle \mathbf{w}_{\ell,D}, \mathbf{x}_{1:D} \rangle + b_{\ell,D}) \cos(w_{D+1}x_{D+1} + a_{D+1}) \\
&= 2^{-D} \sum_{\ell=1}^{2^{D-1}} \{ \cos(\langle \mathbf{w}_{\ell,D}, \mathbf{x}_{1:D} \rangle + b_{\ell,D} + w_{D+1}x_{D+1} + a_{D+1}) \\
&\quad + \cos(\langle \mathbf{w}_{\ell,D}, \mathbf{x}_{1:D} \rangle + b_{\ell,D} - w_{D+1}x_{D+1} - a_{D+1}) \} \\
&= 2^{-D} \sum_{\ell=1}^{2^{D-1}} \{ \cos(\langle (\mathbf{w}_{\ell,D}, w_{D+1}), \mathbf{x} \rangle + b_{\ell,D} + a_{D+1}) + \cos(\langle (\mathbf{w}_{\ell,D}, -w_{D+1}), \mathbf{x} \rangle + b_{\ell,D} - a_{D+1}) \} \\
&= 2^{-D} \sum_{\ell'=1}^{2^D} \cos(\langle (\mathbf{w}_{\ell',D+1}, \mathbf{x}) \rangle + b_{\ell',D+1}),
\end{aligned}$$

where $\mathbf{w}_{\ell',D+1} = (\mathbf{w}_{\lceil \ell'/2 \rceil, D}, (-1)^{\ell'} w_{D+1}) \in \mathcal{W}_{D+1}$, $b_{\ell',D+1} = b_{\lceil \ell'/2 \rceil, D} + (-1)^{\ell'} a_{D+1}$. The proof is completed. \square

Remark 2. As a consequence of Lemma S1, we can write $\psi_k(\mathbf{x})$ in (9) as

$$\psi_k(\mathbf{x}) \propto \frac{1}{|\mathcal{W}_k|} \sum_{\mathbf{w}_{k\ell} \in \mathcal{W}_k} \cos(\langle \mathbf{w}_{k\ell}, \mathbf{x} \rangle + b_{k\ell}), b_{k\ell} \in \mathbb{R},$$

where, with slight abuse of notation, $\mathcal{W}_k = \{(i_{k,1}, c_{\ell 2} i_{k,2}, \dots, c_{\ell D} i_{k,D}) : c_{\ell d} \in \{-1, 1\}, d = 2, \dots, D\}$; $1 \leq k \leq K$ is the index for the k -th tensor product basis; and $b_{k\ell} = a_{k1} + \sum_{d=2}^D c_{\ell d} a_{kd}$ is the corresponding phase to $\mathbf{w}_{k\ell}$; and $a_{kd} = -z_{k,d} \pi / 2$ is the phase for the k -th basis function along the d -th dimension.

Next, we introduce two lemmas that are crucial to the proof for Theorem 1, showing the power functions $\cos(x)^m$ can be written as $\sum_{w \in \mathcal{H}} \cos(wx)$, where the frequency set \mathcal{H} is related to m .

Lemma S2. Denote $\psi_k(\mathbf{x}) = \cos(\langle \mathbf{w}_k, \mathbf{x} \rangle + b_k)$, $\psi_j(\mathbf{x}) = \cos(\langle \mathbf{w}_j, \mathbf{x} \rangle + b_j)$, where $\{\mathbf{w}_k \in \mathbb{Z}^D\}_{k \in \mathcal{K}}$, and $\{\mathbf{w}_j \in \mathbb{Z}^D\}_{j \in \mathcal{J}}$ are two collections of frequency vectors; and $\{b_k \in \mathbb{R}\}_{k \in \mathcal{K}}$ and $\{b_j \in \mathbb{R}\}_{j \in \mathcal{J}}$ are two collections of scalar phases, indexed by $\mathcal{K} = \{1, \dots, K\}$, $\mathcal{J} = \{1, \dots, J\}$. Furthermore, let $\{\beta_{1k} \in \mathbb{R}\}_{k \in \mathcal{K}}$ and $\{\beta_{2j} \in \mathbb{R}\}_{j \in \mathcal{J}}$ be two sets of scalar coefficients and $\mathbf{x} \in \mathbb{T}^D$. Then,

$$\left\{ \sum_{k \in \mathcal{K}} \beta_{1k} \psi_k(\mathbf{x}) \right\} \left\{ \sum_{j \in \mathcal{J}} \beta_{2j} \psi_j(\mathbf{x}) \right\} = \sum_{\tilde{\mathbf{w}} \in \mathcal{D}} \beta_{\tilde{\mathbf{w}}} \psi_{\tilde{\mathbf{w}}}(\mathbf{x}),$$

where $\beta_{\tilde{\mathbf{w}}} = \frac{1}{2}\beta_{1k}\beta_{2j}$, $\psi_{\tilde{\mathbf{w}}}(\mathbf{x}) = \cos(\langle \tilde{\mathbf{w}}, \mathbf{x} \rangle + b_{\tilde{\mathbf{w}}})$, $\mathcal{D} \equiv \mathcal{D}(\{\mathbf{w}_k\}_{k \in \mathcal{K}}, \{\mathbf{w}_j\}_{j \in \mathcal{J}}) = \{\tilde{\mathbf{w}} = \mathbf{w}_k \pm \mathbf{w}_j, k \in \mathcal{K}, j \in \mathcal{J}\}$, and $\tilde{b}_{\tilde{\mathbf{w}}} = b_k + c_{\tilde{\mathbf{w}}}b_j$, with $k, j, c_{\tilde{\mathbf{w}}}$ induced by the form of $\tilde{\mathbf{w}}$, i.e. $c_{\tilde{\mathbf{w}}} = 1$ if $\tilde{\mathbf{w}} = \mathbf{w}_k + \mathbf{w}_j$, and $c_{\tilde{\mathbf{w}}} = -1$ if $\tilde{\mathbf{w}} = \mathbf{w}_k - \mathbf{w}_j$. Note that the cardinality of \mathcal{D} is proportional to $|\mathcal{K}| \times |\mathcal{J}|$.

Proof of Lemma S2.

$$\begin{aligned}
& \left\{ \sum_{k \in \mathcal{K}} \beta_{1k} \psi_k(\mathbf{x}) \right\} \left\{ \sum_{j \in \mathcal{J}} \beta_{2j} \psi_j(\mathbf{x}) \right\} \\
&= \left\{ \sum_{k \in \mathcal{K}} \beta_{1k} \cos(\langle \mathbf{w}_k, \mathbf{x} \rangle + b_k) \right\} \left\{ \sum_{j \in \mathcal{J}} \beta_{2j} \cos(\langle \mathbf{w}_j, \mathbf{x} \rangle + b_j) \right\} \\
&= \sum_{k \in \mathcal{K}} \sum_{j \in \mathcal{J}} \beta_{1k} \beta_{2j} \cos(\langle \mathbf{w}_k, \mathbf{x} \rangle + b_k) \cos(\langle \mathbf{w}_j, \mathbf{x} \rangle + b_j) \\
&= \sum_{k \in \mathcal{K}} \sum_{j \in \mathcal{J}} \frac{1}{2} \beta_{1k} \beta_{2j} \cos(\langle \mathbf{w}_k + \mathbf{w}_j, \mathbf{x} \rangle + b_k + b_j) + \cos(\langle \mathbf{w}_k - \mathbf{w}_j, \mathbf{x} \rangle + b_k - b_j) \\
&= \sum_{\tilde{\mathbf{w}} \in \mathcal{D}} \beta_{\tilde{\mathbf{w}}} \psi_{\tilde{\mathbf{w}}}(\mathbf{x}).
\end{aligned}$$

The proof is completed. \square

Corollary 1. Denote $\psi_k(\mathbf{x}) = \sum_{\ell=1}^{2^{D-1}} \cos(\langle \mathbf{w}_{k\ell}, \mathbf{x} \rangle + b_{k\ell})$, $\psi_j(\mathbf{x}) = \sum_{\ell'=1}^{2^{D-1}} \cos(\langle \mathbf{w}_{j\ell'}, \mathbf{x} \rangle + b_{j\ell'})$, where ℓ, ℓ' index frequencies in the corresponding ψ_k and ψ_j , respectively; $\{\mathbf{w}_{k\ell} \in \mathbb{Z}^D\}_{k \in \mathcal{K}, 1 \leq \ell \leq 2^{D-1}}$ and $\{\mathbf{w}_{j\ell'} \in \mathbb{Z}^D\}_{j \in \mathcal{J}, 1 \leq \ell' \leq 2^{D-1}}$ are two collections of frequency vectors; and $\{b_{k\ell} \in \mathbb{R}\}_{k \in \mathcal{K}}$ and $\{b_{j\ell'} \in \mathbb{R}\}_{j \in \mathcal{J}}$ are two collections of scalar phases, indexed by $\mathcal{K} = \{1, \dots, K\}$, $\mathcal{J} = \{1, \dots, J\}$. Furthermore, let $\{\beta_{1k} \in \mathbb{R}\}_{k \in \mathcal{K}}$ and $\{\beta_{2j} \in \mathbb{R}\}_{j \in \mathcal{J}}$ be two sets of scalar coefficients and $\mathbf{x} \in \mathbb{T}^D$. Then,

$$\left\{ \sum_{k \in \mathcal{K}} \beta_{1k} \psi_k(\mathbf{x}) \right\} \left\{ \sum_{j \in \mathcal{J}} \beta_{2j} \psi_j(\mathbf{x}) \right\} = \sum_{\tilde{\mathbf{w}} \in \mathcal{D}} \beta_{\tilde{\mathbf{w}}} \psi_{\tilde{\mathbf{w}}}(\mathbf{x}),$$

where $\beta_{\tilde{\mathbf{w}}} = \frac{1}{2}\beta_{1k}\beta_{2j}$, $\psi_{\tilde{\mathbf{w}}}(\mathbf{x}) = \cos(\langle \tilde{\mathbf{w}}, \mathbf{x} \rangle + b_{\tilde{\mathbf{w}}})$, $\mathcal{D} \equiv \mathcal{D}(\{\mathbf{w}_{k\ell}\}_{k \in \mathcal{K}}, \{\mathbf{w}_{j\ell'}\}_{j \in \mathcal{J}}) = \{\tilde{\mathbf{w}} = \mathbf{w}_{k\ell} \pm \mathbf{w}_{j\ell'}, k \in \mathcal{K}, j \in \mathcal{J}, 1 \leq \ell, \ell' \leq 2^{D-1}\}$, and $b_{\tilde{\mathbf{w}}} = b_{k\ell} + c_{\tilde{\mathbf{w}}}b_{j\ell'}$, with $k, j, \ell, \ell', c_{\tilde{\mathbf{w}}}$ induced by the form of $\tilde{\mathbf{w}}$. In particular, $c_{\tilde{\mathbf{w}}} = 1$ if $\tilde{\mathbf{w}} = \mathbf{w}_{k\ell} + \mathbf{w}_{j\ell'}$, and $c_{\tilde{\mathbf{w}}} = -1$ if $\tilde{\mathbf{w}} = \mathbf{w}_{k\ell} - \mathbf{w}_{j\ell'}$. Note that the cardinality of \mathcal{D} is proportional to $2^D |\mathcal{K}| |\mathcal{J}|$.

Proof of Corollary 1.

$$\begin{aligned}
& \left\{ \sum_{k \in \mathcal{K}} \beta_{1k} \psi_k(\mathbf{x}) \right\} \left\{ \sum_{j \in \mathcal{J}} \beta_{2j} \psi_j(\mathbf{x}) \right\} \\
&= \left\{ \sum_{k \in \mathcal{K}} \beta_{1k} \sum_{\ell} \cos(\langle \mathbf{w}_{k\ell}, \mathbf{x} \rangle + b_{k\ell}) \right\} \left\{ \sum_{j \in \mathcal{J}} \beta_{2j} \sum_{\ell'} \cos(\langle \mathbf{w}_{j\ell'}, \mathbf{x} \rangle + b_{j\ell'}) \right\} \\
&= \sum_{k \in \mathcal{K}} \sum_{j \in \mathcal{J}} \beta_{1k} \beta_{2j} \sum_{\ell, \ell'} \cos(\langle \mathbf{w}_{k\ell}, \mathbf{x} \rangle + b_{k\ell}) \cos(\langle \mathbf{w}_{j\ell'}, \mathbf{x} \rangle + b_{j\ell'}) \\
&= \sum_{k \in \mathcal{K}} \sum_{j \in \mathcal{J}} \sum_{\ell, \ell'} \frac{1}{2} \beta_{1k} \beta_{2j} \cos(\langle \mathbf{w}_{k\ell} + \mathbf{w}_{j\ell'}, \mathbf{x} \rangle + b_{k\ell} + b_{j\ell'}) + \cos(\langle \mathbf{w}_{k\ell} - \mathbf{w}_{j\ell'}, \mathbf{x} \rangle + b_{k\ell} - b_{j\ell'}) \\
&= \sum_{\tilde{\mathbf{w}} \in \mathcal{D}} \beta_{\tilde{\mathbf{w}}} \psi_{\tilde{\mathbf{w}}}(\mathbf{x})
\end{aligned}$$

The proof is completed. \square

Lemma S3. Let $\{\mathbf{w}_{k\ell} \in \mathbb{R}^D\}_{k \in \mathcal{K}, 1 \leq \ell \leq 2^{D-1}}$ and $\{b_{k\ell} \in \mathbb{R}\}_{k \in \mathcal{K}}$ be a collection of frequency vectors and scalar phases, respectively, indexed by the set $\mathcal{K} = \{1, \dots, K\} \subseteq \mathbb{N}$. Furthermore, $\{\beta_k \in \mathbb{R}\}_{k \in \mathcal{K}}$ be a set of scalar coefficients, and let $m \in \mathbb{N}$. Then,

$$\left(\sum_{k \in \mathcal{K}} \beta_k \sum_{\ell} \cos(\langle \mathbf{w}_{k\ell}, \mathbf{x} \rangle + b_{k\ell}) \right)^m = \sum_{\tilde{\mathbf{w}} \in \mathcal{H}_m} \tilde{\beta}_{\tilde{\mathbf{w}}} \cos(\langle \tilde{\mathbf{w}}, \mathbf{x} \rangle + \tilde{b}_{\tilde{\mathbf{w}}}),$$

where

$$\begin{aligned}
\mathcal{H}_m &= \left\{ \tilde{\mathbf{w}} = \sum_{k=1}^K c_k \mathbf{w}_{k\ell} \mid c_k \in \{n_k, n_k - 2, \dots, -(n_k - 2)\}, \sum_{k=1}^K n_k = m, n_k \in \mathbb{N}, 1 \leq \ell \leq 2^{D-1} \right\} \\
&\equiv \left\{ \tilde{\mathbf{w}} = \sum_{k=1}^K c_k \mathbf{w}_k \mid c_k \in \{n_k, n_k - 2, \dots, -(n_k - 2)\}, \sum_{k=1}^K n_k = m, n_k \in \mathbb{N}, \mathbf{w}_k \in \mathcal{W}_k \right\},
\end{aligned} \tag{S.5}$$

with $n_j \in \mathbb{N}$ being the polynomial degree contributed by the j th frequency. In addition,

$$\mathcal{H}_m \subseteq \tilde{\mathcal{H}}_m = \left\{ \tilde{\mathbf{w}} = \sum_{k \in \mathcal{K}} \sum_{\mu=1}^m c_{k,\mu} \mathbf{w}_k, c_{k,\mu} \in \mathbb{Z} \wedge \sum_{k \in \mathcal{K}} \sum_{\mu=1}^m |c_{k,\mu}| \leq m, \mathbf{w}_k \in \mathcal{W}_k \right\}. \tag{S.6}$$

Note that we use the notation \mathcal{H}_m and $\tilde{\mathcal{H}}_m$ instead of explicitly writing the dependence on the set $(\{\mathbf{w}_{k\ell}\}_{k \in \mathcal{K}, 1 \leq \ell \leq 2^{D-1}})$ for simplicity.

Proof of Lemma S3. The proof of (S.5) is completed by induction.

Base case. When $m = 1$, it is only possible for one $k \in \mathcal{K}$ such that $m = 1$, $c_k = 1$, and $c_{k'} = 0, \forall k' \neq k$. Exhausting all $|\mathcal{K}|$ possibilities would give us all elements in $\mathcal{H}_1 = \{\mathbf{w}_k, k \in \mathcal{K}\}$.

Inductive Step. Suppose the equality holds for m , then we have

$$\begin{aligned}
& \left\{ \sum_{k \in \mathcal{K}} \beta_k \psi_k(\mathbf{x}) \right\}^{m+1} \\
&= \left\{ \sum_{k \in \mathcal{K}} \beta_k \sum_{\ell} \cos(\langle \mathbf{w}_{k\ell}, \mathbf{x} \rangle + b_{k\ell}) \right\}^{m+1} \\
&= \left\{ \sum_{k \in \mathcal{K}} \beta_k \sum_{\ell} \cos(\langle \mathbf{w}_{k\ell}, \mathbf{x} \rangle + b_{k\ell}) \right\}^m \left\{ \sum_{k \in \mathcal{K}} \beta_k \sum_{\ell} \cos(\langle \mathbf{w}_{k\ell}, \mathbf{x} \rangle + b_{k\ell}) \right\} \\
&= \left\{ \sum_{\tilde{\mathbf{w}}_{k\ell} \in \mathcal{H}_m} \tilde{\beta}_k \cos(\langle \tilde{\mathbf{w}}_{k\ell}, \mathbf{x} \rangle + \tilde{b}_{\tilde{\mathbf{w}}_{k\ell}}) \right\} \left\{ \sum_{k' \in \mathcal{K}} \beta_{k'} \sum_{\ell'} \cos(\langle \mathbf{w}_{k'\ell'}, \mathbf{x} \rangle + b_{k'\ell'}) \right\} \\
&= \sum_{\tilde{\mathbf{w}}_{k\ell} \in \mathcal{D}\{\mathcal{H}_m, \{\mathbf{w}_{k'}\}_{k' \in \mathcal{K}}\}} \tilde{\beta}_k \cos(\langle \tilde{\mathbf{w}}_{k\ell}, \mathbf{x} \rangle + \tilde{b}_{\tilde{\mathbf{w}}_{k\ell}}),
\end{aligned}$$

where we used $\cos a \cos b = (\cos(a + b) + \cos(a - b))/2$, and $\tilde{\beta}_k, \tilde{\beta}_k, \tilde{b}_k, \tilde{b}_k$ are constants. By Lemma S2,

$$\begin{aligned}
& \mathcal{D}\{\mathcal{H}_m, \{\mathbf{w}_{k'}\}_{k' \in \mathcal{K}}\} \\
&= \left\{ \mathbf{w}' | \mathbf{w}' = \sum_{k \in \mathcal{K}} c_k \mathbf{w}_{k\ell} \pm \mathbf{w}_{k'\ell'}, c_k \in \{n_k, n_k - 2, \dots, -(n_k - 2)\}, \sum_{k \in \mathcal{K}} n_k = m, n_k \in \mathbb{N} \right\} \\
&= \left\{ \mathbf{w}' | \mathbf{w}' = \sum_{k \in \mathcal{K}} c_k \mathbf{w}_{k\ell} \pm \mathbf{w}_{k'\ell'}, c_k \in \{n_k + 1, n_k - 1, \dots, -(n_k - 1)\}, \sum_{k \in \mathcal{K}} n_k = m, n_k \in \mathbb{N} \right\} \\
&= \left\{ \mathbf{w}' | \mathbf{w}' = \sum_{k \in \mathcal{K}} c_k \mathbf{w}_{k\ell} \pm \mathbf{w}_{k'\ell'}, c_k \in \{n_k, n_k - 2, \dots, -(n_k - 2)\}, \sum_{k \in \mathcal{K}} n_k = m + 1, n_k \in \mathbb{N} \right\} \\
&\equiv \mathcal{H}_{m+1}
\end{aligned}$$

Equation (S.6) holds by definition, since $c_{k,\mu}$ in (S.6) belongs to a larger set than c_k in (S.5). \square

In order to prove Theorem 1, we first prove an analogous Theorem S2, where activation function is a polynomial of degree M , $\alpha^{(l)}(v) = \sum_{\mu=1}^M \beta_\mu v^\mu$, then the space of frequencies of $v_\theta(\mathbf{x})$ is $\mathcal{H}^{(L)}$. The form of $\mathcal{H}^{(L)}$ reveals the power of proposed NF in approximating functions of a rich set of frequencies.

Theorem S2. Let $\mathcal{M}_d = \mathbb{S}^1$, $v_\theta : \mathbb{T}^D = \times_{d=1}^D \mathbb{S}^1 \rightarrow \mathbb{R}$ be an NF of the form (5), with $\eta : \mathbb{T}^D \mapsto \mathbb{R}^K$ whose k^{th} element is defined as (9). Denote the set of frequencies $\mathcal{W}_k = \{(i_{k,1}, \pm i_{k,2}, \dots, \pm i_{k,D})\}$, for $k = 1, \dots, K$. We consider a polynomial activation function $\alpha^{(l)}(v) = \sum_{m=0}^M \beta_m v^m$ for $l > 1$. Let $\mathbf{W}^{(l)} \in \mathbb{R}^{H_l \times H_{l-1}}$ be the matrix of frequencies, and $\mathbf{b}^{(l)} \in \mathbb{R}^{H_l}$ are the vector of phases. Then

$$v_\theta(\mathbf{x}) = \sum_{\mathbf{w}' \in \mathcal{H}^{(L)}} \beta_{\mathbf{w}'} \cos(\langle \mathbf{w}', \mathbf{x} \rangle + b_{\mathbf{w}'}),$$

where

$$\mathcal{H}^{(l)} = \left\{ \tilde{\mathbf{w}} = \sum_{k=1}^K c_k \mathbf{w}_k \mid c_k \in \mathcal{A}^{(l)}, \mathbf{w}_k \in \mathcal{W}_k \right\} \subseteq \left\{ \tilde{\mathbf{w}} = \sum_{k=1}^K c_k \mathbf{w}_k \mid \sum_{k=1}^K |c_k| \leq M^l, \mathbf{w}_k \in \mathcal{W}_k \right\},$$

where $\mathcal{A}^{(l)} = \{c_k = \prod_{i=1}^l c_k^{(i)} \mid c_k^{(i)} \in \mathcal{A}\}$ is a set of integers that contains possible candidates of coefficient c_k , with $\mathcal{A} = \{c_k \in \{n_k, n_k - 2, \dots, -(n_k - 2)\} \mid \sum_{k=1}^K n_k \in \{1, \dots, M\}, n_k \in \mathbb{N}\}$ and $\beta_{\mathbf{w}'}$ are complicated functions of θ .

Proof of Theorem S2. First we note that $\mathcal{H}^{l_1} \subseteq \mathcal{H}^{l_2}$ for any $l_1 \leq l_2$. We prove the theorem by induction. To focus on the frequency representation, we let bias terms $\mathbf{b}^{(l)}$ be zero.

Base case. When $l = 1$, consider the pre-activation of a node at the first layer for any INR in the form of (5). Recall that $\mathbf{W}^{(1)}$ is of dimension $H_1 \times H_0$, where $H_0 = K$. We denote $\mathbf{v}^{(1)} = \mathbf{W}^{(1)}\eta(\mathbf{x})$ as the pre-activation vector of first layer. Specifically, the j -th element of $\mathbf{v}^{(1)}$ is $v_j^{(1)} = \mathbf{W}_j^{(1)}\eta(\mathbf{x}) = \sum_{k=1}^K W_{jk}^{(1)} \psi_k(\mathbf{x}) = \sum_{k=1}^K W_{jk}^{(1)} \sum_{\ell=1}^{2^D-1} \frac{1}{2^D-1} \cos(\langle \mathbf{w}_{k\ell}, \mathbf{x} \rangle + b_{k\ell})$.

Applying Lemma S3, the output of this node after activation is

$$\begin{aligned} z_j^{(1)} &= \alpha^{(1)}(v_j^{(1)}) = \sum_{m=0}^M \beta_m (v_j^{(1)})^m \\ &= \sum_{m=0}^M \beta_m \left(\sum_{k=1}^K W_{jk}^{(1)} \sum_{\ell=1}^{2^D-1} \frac{1}{2^D-1} \cos(\langle \mathbf{w}_{k\ell}, \mathbf{x} \rangle + b_{k\ell}) \right)^m \\ &= \sum_{m=0}^M \beta_m \sum_{\tilde{\mathbf{w}} \in \mathcal{H}_m} \tilde{\beta}_{\tilde{\mathbf{w}},j} \cos(\langle \tilde{\mathbf{w}}, \mathbf{x} \rangle + \tilde{b}_{\tilde{\mathbf{w}},j}) \\ &= \sum_{\tilde{\mathbf{w}} \in \mathcal{H}^{(1)}} \tilde{\beta}_{\tilde{\mathbf{w}},j} \cos(\langle \tilde{\mathbf{w}}, \mathbf{x} \rangle + \tilde{b}_{\tilde{\mathbf{w}},j}). \end{aligned}$$

Induction Step. Assume the output of the nodes at layer l satisfy the following expression:

$$h_j^{(l)} = \sum_{\tilde{\mathbf{w}} \in \mathcal{H}^{(l)}} \tilde{\beta}_{\tilde{\mathbf{w}},j} \cos(\langle \tilde{\mathbf{w}}, \mathbf{x} \rangle + \tilde{b}_{\tilde{\mathbf{w}},j}).$$

Then, the pre-activation of the j^{th} node at the $(l+1)^{\text{th}}$ layer can be expressed as $v_j^{(l+1)} = \sum_{\mathbf{w} \in \mathcal{H}^{(l)}} \beta_{\mathbf{w},j} \cos(\langle \mathbf{w}, \mathbf{x} \rangle + \tilde{b}_{\mathbf{w},j})$, with $\beta_{\mathbf{w},j}$ being different from $\tilde{\beta}_{\tilde{\mathbf{w}},j}$. Applying the activation function to the output of the j^{th} node at the $(l+1)^{\text{th}}$ layer, we have

$$\begin{aligned} h_j^{(l+1)} &= \alpha^{(l+1)}(v_j^{(l+1)}) = \sum_{m=0}^M \beta_m (v_j^{(l+1)})^m = \sum_{m=0}^M \beta_m \left(\sum_{\mathbf{w} \in \mathcal{H}^{(l)}} \beta_{\mathbf{w},j} \cos(\langle \mathbf{w}, \mathbf{x} \rangle + \tilde{b}_{\mathbf{w},j}) \right)^m \\ &= \sum_{m=0}^M \beta_m \sum_{\mathbf{w}' \in \mathcal{H}_m^{(l)}} \tilde{\beta}_{\mathbf{w}',j} \cos(\langle \mathbf{w}', \mathbf{x} \rangle + \tilde{b}_{\mathbf{w}',j}), \end{aligned}$$

where

$$\begin{aligned} \mathcal{H}_m^{(l)} &= \left\{ \mathbf{w} \mid \mathbf{w} = \sum_{k=1}^K c_k \mathbf{w}_k, \mathbf{w}_k \in \mathcal{H}^{(l)}, c_k \in \{n_k, n_k - 2, \dots, -(n_k - 2)\}, \sum_{k=1}^K n_k = m, n_k \in \mathbb{N} \right\} \\ &= \left\{ \mathbf{w} \mid \mathbf{w} = \sum_{k=1}^K c_k \sum_{k=1}^K \{\prod_{l=1}^l \tilde{c}_k^{(l)}\} \mathbf{w}_k, \tilde{c}_k^{(l)} \in \mathcal{A}, c_k \in \mathcal{B}_m, n_k \in \mathbb{N}, \mathbf{w}_k \in \mathcal{W}_k \right\}, \end{aligned}$$

where $\mathcal{B}_m = \{c_k \in \{n_k, n_k - 2, \dots, -(n_k - 2)\}, \sum_{k=1}^K n_k = m\}$. By construction, we know that $\cup_{m=1}^M \mathcal{B}_m = \mathcal{A}$, and $\cup_{m=1}^M \mathcal{H}_m^{(l)} = \mathcal{H}^{(l+1)}$, therefore,

$$h_j^{(l+1)} = \sum_{\mathbf{w}' \in \mathcal{H}^{(l+1)}} \tilde{\beta}_{\mathbf{w}',j} \cos(\langle \mathbf{w}', \mathbf{x} \rangle + \tilde{b}_{\mathbf{w}',j}).$$

The proof is complete by setting $l = L$. \square

Proof. Proof of Theorem 1. We prove Theorem 1 by approximating the activation function $\alpha^{(l)}(v) = \sin(v)$ using polynomials and Theorem S2.

First we note for any v in the neighborhood of zero, $\sin(v) = \sum_{m=0}^M (-1)^m v^{2m+1} / (2m+1)! + \varepsilon$, where $\varepsilon = (-1)^{M+1} \xi^{2M+3} / (2M+3)!$, and ξ is a constant between 0 and v . We have $|\varepsilon| \leq |\xi|^{2M+3} / (2M+3)! \leq |v|^{2M+3} / (2M+3)!$.

Due to the activation function $\sin(\cdot)$, we have $|\mathbf{h}^{(l-1)}| \leq 1, 2 \leq l \leq N$. At layer l , since $|\mathbf{W}^{(l)}| < C_w$ and $|\mathbf{b}^{(l)}| < C_b$ for some finite constant $0 < C_w, C_b < \infty$, we have pre-activation value $\mathbf{v}^{(l)} = \mathbf{W}^{(l)} \mathbf{h}^{(l-1)} + \mathbf{b}^{(l)}$ bounded, i.e. $|\mathbf{v}^{(l)}| < C_w + C_b$. The j^{th} entry of $\mathbf{v}^{(l)}$ is denoted by $v_j^{(l)}$, and the j^{th} node after activation takes the form $h_j^{(l)} = \sin(v_j^{(l)}) = \sum_{m=0}^M (-1)^m (v_j^{(l)})^{2m+1} / (2m+1)! + \varepsilon_j^{(l)}$, where $\varepsilon_j^{(l)} = (-1)^{M+1} (\xi_j^{(l)})^{2M+3} / (2M+3)!$, and $|\xi_j^{(l)}| < (C_w + C_b)$.

At the $(l+1)^{\text{th}}$ layer, pre-activation node is $\mathbf{v}^{(l+1)} = \mathbf{W}^{(l+1)} \mathbf{h}^{(l)} + \mathbf{b}^{(l+1)}$ and its approximation $\tilde{\mathbf{v}}^{(l+1)} = \mathbf{W}^{(l+1)} \tilde{\mathbf{h}}^{(l)} + \mathbf{b}^{(l+1)} = \mathbf{W}^{(l+1)} (\mathbf{h}^{(l)} + \boldsymbol{\varepsilon}^{(l)}) + \mathbf{b}^{(l+1)}$, where $|\boldsymbol{\varepsilon}^{(l)}| < \epsilon$. The node

after activation is $\mathbf{h}^{(l+1)} = \sin(\mathbf{v}^{(l+1)})$ and its approximation $\tilde{h}_j^{(l+1)} = \sum_{m=0}^M (-1)^m \tilde{v}_j^{(l+1)} / (2m+1)! + (-1)^{M+1} (\xi_j^{(l+1)})^{2M+3} / (2M+3)!$. The approximation error can be decomposed into two parts

$$\begin{aligned} \varepsilon_j^{(l+1)} &= h_j^{(l+1)} - \tilde{h}_j^{(l+1)} \\ &= \sin(v_j^{(l+1)}) - \widetilde{\sin}(\tilde{v}_j^{(l+1)}) \\ &= \{\sin(v_j^{(l+1)}) - \sin(\tilde{v}_j^{(l+1)})\} + \{\sin(\tilde{v}_j^{(l+1)}) - \widetilde{\sin}(\tilde{v}_j^{(l+1)})\} \\ &= I + II, \end{aligned}$$

where $\widetilde{\sin}$ indicates the polynomial approximation to \sin . It can be shown that $|I| \leq C_w |\varepsilon_j^{(l)}|$, and $|II| \leq (C_w + C_b)^{2M+3} / (2M+3)!$.

By induction, at the $(L-1)^{th}$ layer, $|h_j^{(L-1)} - \tilde{h}_j^{(L-1)}| \lesssim C_w^{L-2} (C_w + C_b)^{2M+3} / (2M+3)!$. Suppose the maximal tolerance for the approximation error of $\tilde{h}_j^{(L-1)}$ for $h_j^{(L-1)}$ is ϵ , then the minimal degree of polynomial activation function for all interior layers is $M_\epsilon = \min\{m : C_w^{L-2} (C_w + C_b)^{2m+3} / (2m+3)! < \epsilon\}$. Note that for any integer m , $\lim_{m \rightarrow \infty} C^m / m! = 0$ holds for any finite constant C . Therefore M_ϵ is finite and exists, such that approximation error of polynomial to sine function can be controlled. \square

S2 Geometry

S2.1 \mathbb{S}^1

We can parameterize $\mathbb{S}^1 \subset \mathbb{R}^2$ using $\gamma \in [0, 2\pi)$ via the map $l(\gamma) \mapsto (\cos(\gamma), \sin(\gamma))$. The tangent vector is then given by $\partial_\gamma l(\gamma) = (-\sin(\gamma), \cos(\gamma))$, hence the induced Riemannian metric is given by $G_{\gamma\gamma} = \langle \partial_\gamma l(\gamma), \partial_\gamma l(\gamma) \rangle = \sin^2(\gamma) + \cos^2(\gamma) = 1$. Denoting $v : \mathbb{S}^1 \mapsto \mathbb{R}^1$, then by definition the Laplace-Beltrami operator under the induced Riemannian metric $G_{\gamma\gamma}$ simplifies to $\Delta_{\mathbb{S}^1}[v] = \frac{1}{\sqrt{\det G_{\gamma\gamma}}} \frac{\partial}{\partial \gamma} (\sqrt{\det G_{\gamma\gamma}} G_{\gamma\gamma}^{-1} \frac{\partial v}{\partial \gamma}) = \frac{\partial^2 v}{\partial \gamma^2}$. The operator equation (6) then takes the form

$$\frac{\partial^2 \phi_k}{\partial \gamma^2} = -\lambda_k \phi_k.$$

We assume the solution takes the form $\phi_k(\gamma) = \exp(\mu_k \gamma)$, for constant μ_k to be found, resulting in $\mu_k^2 \exp(\mu_k \gamma) = -\lambda_k \exp(\mu_k \gamma)$, which results in the characteristic equation $\mu_k^2 = -\lambda_k$. We know that λ_k are non-negative, hence we have two cases.

1) $\lambda_k > 0$: which gives roots $\mu_k = \pm i\sqrt{\lambda_k}$, implying solutions $\{\exp(i\sqrt{\lambda_k}\gamma), \exp(-i\sqrt{\lambda_k}\gamma)\}$.

It is well known that by Euler's formula, we have the real part of these solutions given as $\{\cos(\sqrt{\lambda_k}\gamma), \sin(\sqrt{\lambda_k}\gamma)\}$. Hence, all solutions are of the form $\phi_k(\gamma) = A \cos(\sqrt{\lambda_k}\gamma) + B \sin(\sqrt{\lambda_k}\gamma)$, for some constants A and B . Since ϕ_k is a function on \mathbb{S}^1 , we know that $\phi_k(0) = \phi_k(2\pi)$ and $\frac{\partial\phi_k}{\partial\gamma}(0) = \frac{\partial\phi_k}{\partial\gamma}(2\pi)$. These can be used to form sets of equations for determining λ_k via

$$\begin{aligned} A &= A \cos(2\pi\sqrt{\lambda_k}) + B \sin(2\pi\sqrt{\lambda_k}) \\ B\sqrt{\lambda_k} &= -A\sqrt{\lambda_k} \sin(2\pi\sqrt{\lambda_k}) + B\sqrt{\lambda_k} \cos(2\pi\sqrt{\lambda_k}). \end{aligned}$$

Refactoring the system of equations and writing them in matrix form gives:

$$\begin{pmatrix} 1 - \cos(2\pi\sqrt{\lambda_k}) & -\sin(2\pi\sqrt{\lambda_k}) \\ \sin(2\pi\sqrt{\lambda_k}) & 1 - \cos(2\pi\sqrt{\lambda_k}) \end{pmatrix} \begin{pmatrix} A \\ B \end{pmatrix} = \begin{pmatrix} 0 \\ 0 \end{pmatrix}$$

For non-trivial solutions, the matrix must be singular and hence have zero determinant, which implies

$$\begin{aligned} 0 &= (1 - \cos(2\pi\sqrt{\lambda_k}))^2 + \sin^2(2\pi\sqrt{\lambda_k}) \\ &= 1 - 2\cos(2\pi\sqrt{\lambda_k}) + \cos^2(2\pi\sqrt{\lambda_k}) + \sin^2(2\pi\sqrt{\lambda_k}) \\ &= 2 - 2\cos(2\pi\sqrt{\lambda_k}) \end{aligned}$$

Hence, we have that $\sqrt{\lambda_k}$ must satisfy

$$\cos(2\pi\sqrt{\lambda_k}) = 1,$$

which implies $\sqrt{\lambda_k} \in \mathbb{Z}$, or equivalently that $\lambda_k = k^2$ for $k \in \mathbb{Z}$. Since we want our eigenfunctions to be orthonormal, i.e., $\|\phi_k\|_{L^2(\mathbb{S}^1)} = 1$, using the fact that $\int_{\mathbb{S}^1} \sin^2(k\gamma) d\gamma = \int_{\mathbb{S}^1} \cos^2(k\gamma) d\gamma = \pi, \forall k \in \mathbb{R}$, this implies $A = B = \frac{1}{\sqrt{\pi}}$. Hence, we have 2 linearly independent eigenfunctions $\{\frac{\cos(k\gamma)}{\sqrt{\pi}}, \frac{\sin(k\gamma)}{\sqrt{\pi}}\}$ corresponding to eigenvalue k^2 , for $k \in \mathbb{Z}$.

2) For $\lambda_k = 0$, we have the constant eigenfunction. The orthonormality condition enforces this eigenfunction, denoted $\phi_0 = \frac{1}{\sqrt{2\pi}}$.

S2.2 \mathbb{S}^2

A local parameterization of $\mathbb{S}^2 \subset \mathbb{R}^3$ that is smooth and bijective (outside the poles) is

$$l(\gamma_1, \gamma_2) = (\sin(\gamma_1) \cos(\gamma_2), \sin(\gamma_1) \sin(\gamma_2), \cos(\gamma_1))^T,$$

which is valid (invertible) for all points on \mathbb{S}^2 except $(0, 0, \pm 1)$. In this parameterization, γ_1 is the inclination and γ_2 is the azimuth angle. By definition, the vectors

$$\begin{aligned} t_1 &:= \frac{\partial l}{\partial \gamma_1}(\gamma_1, \gamma_2) = (\cos(\gamma_1) \cos(\gamma_2), \cos(\gamma_1) \sin(\gamma_2), -\sin(\gamma_1))^\top \\ t_2 &:= \frac{\partial l}{\partial \gamma_2}(\gamma_1, \gamma_2) = (-\sin(\gamma_1) \sin(\gamma_2), \sin(\gamma_1) \cos(\gamma_2), 0)^\top \end{aligned} \tag{S.7}$$

form an orthogonal basis for the tangent space $T_x(\mathbb{S}^2)$. The induced Riemannian metric is given by $G \in \mathbb{R}^{2 \times 2}$ with element-wise definition $G_{i,j}(\gamma_1, \gamma_2) = \langle t_i, t_j \rangle$. Denoting $v : \mathbb{S}^2 \mapsto \mathbb{R}$, the Laplace-Beltrami operator under the induced Riemannian metric can be calculated as

$$\Delta_{\mathbb{S}^2}[v] = \frac{1}{\sqrt{|\det G(\gamma_1, \gamma_2)|}} \sum_{i,j} \frac{\partial}{\partial \gamma_i} G_{ij}^{-1}(\gamma_1, \gamma_2) \sqrt{|\det G(\gamma_1, \gamma_2)|} \frac{\partial v}{\partial \gamma_i}(\gamma_1, \gamma_2).$$

The eigenfunctions of $\Delta_{\mathbb{S}^2}$ are the spherical harmonics. In extrinsic (Euclidean) coordinates, they take the form of harmonic homogenous polynomials restricted to \mathbb{S}^2 . Under their common parameterization using spherical coordinates, they have the analytic form:

$$Y_l^m(\gamma_1, \gamma_2) = \sqrt{\frac{(2l+1)(l-m)!}{4\pi(l+m)!}} P_l^m(\cos(\gamma_1)) e^{im\gamma_2}; \quad \gamma_1 \in [0, \pi], \gamma_2 \in [0, 2\pi],$$

where P_m^l are the Legendre polynomials with degree $l = 0, 1, \dots$, and order $m = -l, \dots, 0, \dots, l$. A real-valued set of spherical harmonics that is complete for $L^2(\mathbb{S}^2)$ can be constructed according to

$$\phi_j = \begin{cases} \sqrt{2} \operatorname{Re}(Y_k^m) & -k \leq m < 0 \\ Y_k^0 & m = 0 \\ \sqrt{2} \operatorname{Im}(Y_k^m) & 0 < m \leq k \end{cases}$$

for $k = 0, 1, \dots, l$, $m = -k, \dots, 0, \dots, k$ and $j = k^2 + k + m + 1$. For any finite maximum degree l , the total number of basis functions is $m = (l+1)^2$.

S3 Supporting Methodological Details

S3.1 Architecture

Figure S1 provides an illustration of the proposed architecture for deep product manifold density modeling.

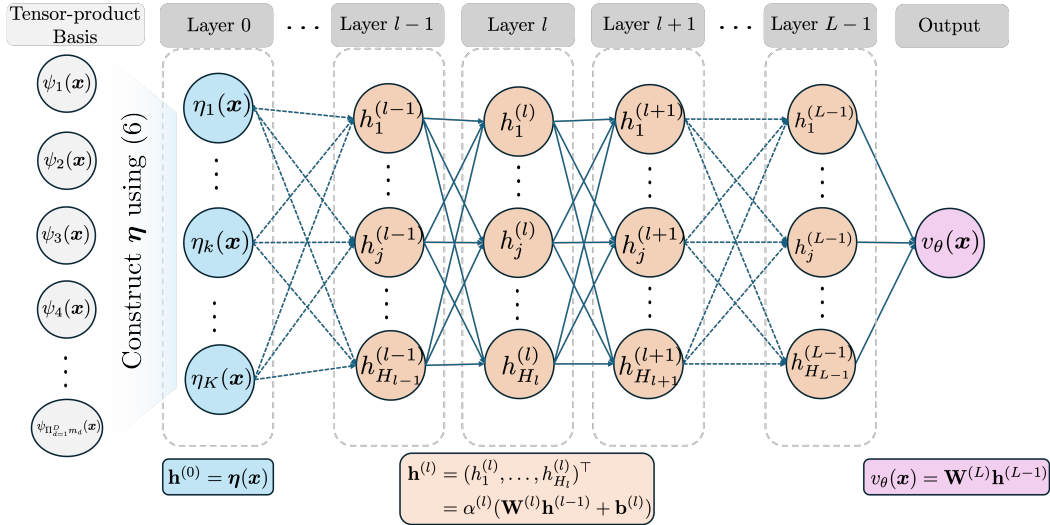


Figure S1: Illustration of proposed MLP architecture.

S3.2 Algorithm Implementation Details

We provide several remarks below to address key implementation details and practical considerations for the Algorithm 1’s successful deployment.

Learning Rate Schedule: In our experiments, for relatively low dimensional cases ($p_d = 1, D \leq 3$), a small fixed learning rate was typically sufficient for fast and stable convergence. For the higher dimensional cases $p_d \geq 2$ and/or $D > 3$, we found a fixed learning rate often leads to relatively slow algorithmic convergence. To accelerate convergence in these cases, we employ a cyclic learning rate schedule under the triangular policy from Smith (2017), which adaptively cycles the learning rate between upper and lower bounds on a fixed schedule and has been observed empirically to improve training speeds dramatically (Smith and Topin, 2019).

Monte-Carlo Integration Sampling: Line 7 in Algorithm 1 requires sampling the uniform distribution over each \mathcal{M}_d . For many manifolds of interest, e.g. \mathbb{S}^p , fast exact procedures are available. If \mathcal{M}_d is represented via triangulation, fast approximate methods exist that only require uniform sampling within the triangles and then weighting by their volumes (Osada et al., 2002). Higher dimensional and non-standard marginal manifolds may require more computationally intensive methods for sampling, e.g. MCMC (Zappa et al., 2018). However, since the gradients in Equation (11) are unbiased for any q_1 and q_2 , smaller values can potentially be used in such cases to reduce computational demands,

albeit at the expense of increased variance.

Derivative Computation While automatic differentiation can be used in the calculation of the roughness penalty gradient as outlined in Section 4.1, this approach requires including the spatial locations of the evaluation points in the computational graph, which may become inefficient for large (deep) networks and large q_2 . In such cases, it may be preferable to approximate the operators using standard Euclidean finite difference schemes, as this only requires forward passes through the network.

S3.3 Non-Separable First-Layer Encoding for \mathbb{T}^D

Let $\mathbb{T}^D = \times_{d=1}^D \mathbb{S}^1$. For a fixed eigenvalue λ of $\Delta_{\mathbb{T}^D}$, taking the tensor products of the marginal eigenfunctions, we have that the eigenfunctions are given by:

$$\boldsymbol{\psi}_\lambda := \left(\pi^{-D/2} \prod_{d=1}^D \cos(i_d x_d - \frac{z_d \pi}{2}), (z_1, \dots, z_D) \in \{0, 1\}^D, \mathbf{i} \in \mathcal{I}_\lambda \right), \quad (\text{S.8})$$

with index set \mathcal{I}_λ defined as in Section 3.1. Define the function

$$\tilde{\boldsymbol{\psi}}_\lambda := \left(\pi^{-D/2} h\left(\sum_{d=1}^D i_d x_d\right) : \mathbf{i} \in \mathcal{I}, h \in \{\sin, \cos\} \right). \quad (\text{S.9})$$

We want to show that there exists a rotation matrix $\mathbf{A}_\lambda \neq \mathbf{I}$ such that $\tilde{\boldsymbol{\psi}}_\lambda = \mathbf{A}_\lambda \boldsymbol{\psi}_\lambda$. That is, $\tilde{\boldsymbol{\psi}}_\lambda$ is a non-separable basis for eigenspace λ with $\text{span}(\tilde{\boldsymbol{\psi}}_\lambda) = \text{span}(\boldsymbol{\psi}_\lambda)$. This can be established by proving the following four facts: 1) All functions in (S.8) and (S.9) are eigenfunctions of $\Delta_{\mathbb{T}^D}$ for fixed eigenvalue λ . 2) The rank of basis (S.8) and (S.9) are equal. 3) The functions in (S.9) are pairwise orthonormal. 4) Any element in (S.9) can be written as a linear combination of elements in (S.8). The proofs for 1-4 proceed as follows:

1. This follows directly from the facts $\frac{\partial^2}{\partial x_d^2} \sin(\sum_{d=1}^D i_d x_d) = -i_d^2 \sin(\sum_{d=1}^D i_d x_d)$ and $\frac{\partial^2}{\partial x_d^2} \cos(\sum_{d=1}^D i_d x_d) = -i_d^2 \cos(\sum_{d=1}^D i_d x_d)$. Hence, all coordinate functions in (S.8) and (S.9) are eigenfunctions of $\Delta_{\mathbb{T}^D}$ with the same eigenvalue, namely $\lambda = \sum_{d=1}^D i_d^2$.
2. (S.9) and (S.8) have the same number of functions. This is due to the fact they are indexed by the same condition $i_1^2, \dots, i_d^2 = \lambda$, for $(i_1, \dots, i_D) \in \mathbb{Z}^D$, with a multiplicative factor of 2 coming from the choice between sin and cosine.

3. The elements of (S.9) are pairwise orthonormal. This can be established from the following standard sum to product identities:

$$\begin{aligned}\sin\left(\sum_{d=1}^D i_d x_d\right) \sin\left(\sum_{d=1}^D i'_d x_d\right) &= \frac{1}{2} \left[\cos\left(\sum_{d=1}^D (i_d - i'_d) x_d\right) - \cos\left(\sum_{d=1}^D (i_d + i'_d) x_d\right) \right] \\ \cos\left(\sum_{d=1}^D i_d x_d\right) \cos\left(\sum_{d=1}^D i'_d x_d\right) &= \frac{1}{2} \left[\cos\left(\sum_{d=1}^D (i_d + i'_d) x_d\right) + \cos\left(\sum_{d=1}^D (i_d - i'_d) x_d\right) \right] \\ \sin\left(\sum_{d=1}^D i_d x_d\right) \cos\left(\sum_{d=1}^D i'_d x_d\right) &= \frac{1}{2} \left[\sin\left(\sum_{d=1}^D (i_d + i'_d) x_d\right) + \sin\left(\sum_{d=1}^D (i_d - i'_d) x_d\right) \right],\end{aligned}$$

and hence the integrals are clearly zero since $i_d - i'_d \in \mathbb{Z}$.

4. That any element in (S.9) can be written as a linear combination of elements in (S.8) can be established by induction.

For $D = 2$, this holds using standard sum and difference formulas

$$\begin{aligned}\cos(i_1 x_1 + i_2 x_2) &= \cos(i_1 x_1) \cos(i_2 x_2) - \sin(i_1 x_1) \sin(i_2 x_2) \\ \sin(i_1 x_1 + i_2 x_2) &= \sin(i_1 x_1) \cos(i_2 x_2) + \cos(i_1 x_1) \sin(i_2 x_2)\end{aligned}$$

Assuming this holds for D . Then for $D + 1$ we again invoke the sum and difference formulas

$$\begin{aligned}\cos\left(\sum_{d=1}^D i_d x_d + i_{D+1} x_{D+1}\right) &= \cos\left(\sum_{d=1}^D i_d x_d\right) \cos(i_{D+1} x_{D+1}) - \sin\left(\sum_{d=1}^D i_d x_d\right) \sin(i_{D+1} x_{D+1}) \\ \sin\left(\sum_{d=1}^D i_d x_d + i_{D+1} x_{D+1}\right) &= \sin\left(\sum_{d=1}^D i_d x_d\right) \cos(i_{D+1} x_{D+1}) + \cos\left(\sum_{d=1}^D i_d x_d\right) \sin(i_{D+1} x_{D+1}).\end{aligned}\tag{S.10}$$

From the induction hypothesis, $\sin(\sum_{d=1}^D i_d x_d)$ and $\cos(\sum_{d=1}^D i_d x_d)$ can be written as a linear combination of separable marginal functions, hence the RHS of (S.10) is also a linear combination of separable marginal functions

This establishes that there exists a rotation matrix \mathbf{A}_λ such that the non-separable eigenbasis functions $\tilde{\psi}_\lambda = \mathbf{A}_\lambda \psi_\lambda$, hence forming a complete and orthonormal basis for the eigenspace corresponding to λ .

Figure S2 plots two randomly selected basis functions for both separable and non-separable formulations for \mathbb{T}^2 . Notice that, due to the separable structure, all basis functions in (S.8) have oscillations only in the marginal directions, i.e. along the coordinate axis

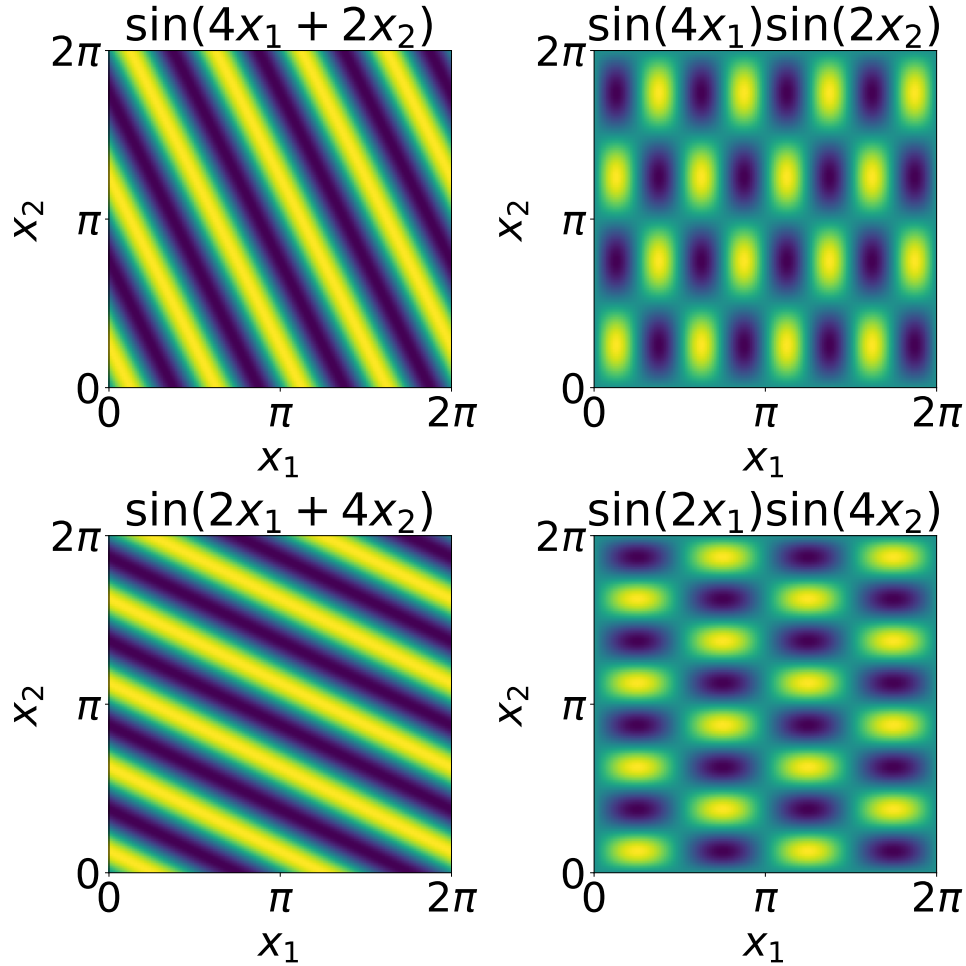


Figure S2: Two non-separable eigenfunctions (left column) and separable eigenfunctions (right column) of $\Delta_{\mathbb{T}^2}$ for the same eigenspace $\lambda = 20$.

for each copy of \mathbb{S}^1 , while the functions from (S.9) have oscillations over varying “diagonal” directions in \mathbb{T}^D . See Section S5.1.3 for an empirical comparison of the impact of separable and non-separable encodings on network convergence.

S4 Tensor Product Basis Density Estimator

With a slight change of notation for clarity, denote the truncation of the marginal eigenfunctions of $\Delta_{\mathcal{M}_d}$ as $\phi_d := (\phi_{d,1}, \dots, \phi_{d,r_d})$, where r_d is the rank. The tensor product basis estimator is a special case of (5) for the following specification:

1. $\boldsymbol{\eta} := \bigotimes_{d=1}^D \phi_d$, i.e. the full set of tensor product functions with $K = \prod_{d=1}^D r_d$

2. $L = 1$, so $\boldsymbol{\theta} := \mathbf{W}^{(1)} \in \mathbb{R}^{\prod_{d=1}^D r_d \times 1}$ and

$$v_{\boldsymbol{\theta}}(x_1, \dots, x_D) = \boldsymbol{\theta}^\top \boldsymbol{\eta}(x_1, \dots, x_D)$$

and hence the task is to find the coefficients $\boldsymbol{\theta}$. WLOG, assume $r_1 = r_2 = \dots = r_D = r$, so $\boldsymbol{\theta} \in \mathbb{R}^{r^D}$. Plugging this representation into (10), we get the optimization problem:

$$\hat{\boldsymbol{\theta}} = \max_{\boldsymbol{\theta} \in \mathbb{R}^{r^D}} \left(\frac{1}{n} \sum_{i=1}^n \boldsymbol{\theta}^\top \boldsymbol{\eta}(x_{1i}, \dots, x_{Di}) - \int_{\Omega} \exp(\boldsymbol{\theta}^\top \boldsymbol{\eta}) d\omega - R_{\tau}(\boldsymbol{\theta}^\top \boldsymbol{\eta}) \right). \quad (\text{S.11})$$

Under the linear basis expansion, the penalty term in (S.11) takes on a special form given by

$$R_{\tau}(\boldsymbol{\theta}^\top \boldsymbol{\eta}) = \tau \int_{\Omega} [\Delta_{\Omega} \boldsymbol{\theta}^\top \boldsymbol{\eta}]^2 d\omega = \tau \boldsymbol{\theta}^\top \left[\int_{\Omega} \Delta_{\Omega} \boldsymbol{\eta} [\Delta_{\Omega} \boldsymbol{\eta}]^\top d\omega \right] \boldsymbol{\theta} := \tau \boldsymbol{\theta}^\top \mathbf{F} \boldsymbol{\theta} \quad (\text{S.12})$$

where $\mathbf{F} \in \mathbb{R}^{r^D \times r^D}$ is the matrix of inner products of the LBO of the encoding function. Due to the fact that $\boldsymbol{\eta}$ are eigenfunctions, \mathbf{F} is a diagonal matrix with elements given by the sums of eigenvalues $\sum_{d=1}^D \lambda_{id}$. Notice that $\exp(\boldsymbol{\theta}^\top \boldsymbol{\eta}(x_1, \dots, x_D))$ is convex in $\boldsymbol{\theta}$, hence $\int_{\Omega} \exp(\boldsymbol{\theta}^\top \boldsymbol{\eta}) d\omega$ is also convex in $\boldsymbol{\theta}$ (Boyd and Vandenberghe, 2004). Using this fact and the convexity of the quadratic form of (S.12), the optimization problem (S.11) is a sum of convex functions, and hence is convex (in $\boldsymbol{\theta}$). Then under some conditions on the decay of the learning rate (Bottou et al., 2018), Algorithm (1) is guaranteed to converge.

S5 Additional Empirical Results

S5.1 Simulation Studies

S5.1.1 Synthetic Data Generation

The true density functions were defined as equally-weighted mixtures of anisotropic wrapped normal distributions (Mardia and Jupp, 2009). The covariance matrices for each mixture component were defined using a parameter *anisotropy-factor* $\in [0, \infty)$, which defines the ratio between the maximum and minimum eigenvalue, hence controlling the degree of local anisotropy. Specifying different anisotropy-factors for different mixture components allows us to simulate density functions with spatially varying anisotropy. Specifically, the covariance matrices were created for each mixture component as follows:

1. A random $D \times D$ orthogonal matrix \mathbf{Q} was sampled.

2. For a pre-defined anisotropy-factor, eigenvalues were calculated according to a logarithmically spaced grid from $\{1, \dots, \text{anisotropy-factor}\}$ and collected to form the diagonal matrix Λ .
3. The covariance matrix was calculated as $\mathbf{C} = \frac{\mathbf{Q}\Lambda\mathbf{Q}^\top}{\max_{ij}[\mathbf{Q}\Lambda\mathbf{Q}^\top]_{ij}}$, where $\max_{ij}[\mathbf{M}]_{ij}$ returns the maximum over all elements in the matrix \mathbf{M} .

For \mathbb{T}^2 , we set the number of mixture components to three with means $(\pi, \pi/2)$, $(\pi, 5\pi/3)$, $(\pi/4, \pi)$ and anisotropy-factors 100, 100, 20, respectively. For \mathbb{T}^4 , we used five components with mean vectors: $(0.5, 0.5, 0.5, 0.5)$, (π, π, π, π) , $(\pi/2, 3\pi/2, 3\pi/2, \pi/2)$, $(3\pi/2, \pi/2, \pi/2, 3\pi/2)$, $(\pi/4, \pi/4, 7\pi/4, 7\pi/4)$, with anisotropy-factors 100, 100, 20, 50, 75, respectively.

S5.1.2 Comparison to ReLU MLP Model

MLP-based neural fields with standard ReLU activations are known to suffer from spectral bias, often facing significant difficulties in training and exhibiting poor convergence in the high-frequency components of the underlying function (Rahaman et al., 2019). However, to our knowledge, most empirical evaluations of this effect have been conducted within the context of L^2 -based learning, which is not our setting. To investigate this behavior in our case, we substituted the network architecture (5) with a “vanilla” ReLU MLP, where all hidden activations are ReLU functions and the initial encoding layer is the identity:

$$\begin{aligned} \mathbf{h}^{(0)} &= \mathbf{x}, \\ \mathbf{h}^{(l)} &= \sigma(\mathbf{W}^{(l)}\mathbf{h}^{(l-1)} + \mathbf{b}^{(l)}), \quad \text{for } l = 1, \dots, L-1, \\ v_\theta(\mathbf{x}) &= \mathbf{W}^{(L)}\mathbf{h}^{(L-1)}, \end{aligned}$$

where σ is the ReLU function. For a fair comparison, we used the same network depth, width, and training algorithm configuration outlined in Section 5.1 and evaluated the model on the same synthetic data. The one difference was that, instead of applying a roughness penalty to enforce regularity, we utilized early stopping, as the ReLU network is no longer second-order differentiable. The early stopping iteration T was selected using the same ISE criteria defined in equation (13) on a small held out validation set. Table S1 provides the results for both \mathbb{T}^2 and \mathbb{T}^4 cases. We see that the ReLU MLP performs poorly in both

ReLU MLP		
\mathbb{T}^2	FR	$1.665 \pm 4.37 \times 10^{-3}$
	nISE	$0.956 \pm 2.96 \times 10^{-3}$
\mathbb{T}^4	FR	$1.540 \pm 1.558 \times 10^{-2}$
	nISE	$0.980 \pm 4.70 \times 10^{-4}$

Table S1: Monte Carlo average simulation results for ReLU MLP with encoding $\eta(\mathbf{x}) = \mathbf{x}$.

cases compared to all estimators considered in the main text (see Table 1). Given that such ReLU networks are universal approximators in the wide-width limit, these results highlight the importance of carefully designing architectures to ensure fast and stable convergence to a quality solution in practice, effectively mitigating spectral bias.

S5.1.3 First-Layer Encodings and Spectral Bias

In this section, we examine the spectral bias of the random separable LBO encoding (S.8) and the rotated random non-separable LBO encoding (S.9), both integrated into identical network architectures and trained under the same parameterization of optimization Algorithm 1 for $T = 5,000$ iterations, using an identical fixed learning rate schedule to ensure a fair comparison. We evaluate the convergence of the networks on randomly selected replications for both the \mathbb{T}^2 and \mathbb{T}^4 synthetic data discussed in Section 5.1. Due to the randomness in both Algorithm 1 and network model (5), the optimization was repeated 5 times with different randomization seeds for both synthetic examples. Every 10 iterations during each training run, the current parameter estimate θ^c was used to calculate the FR error with the ground truth density.

Figure S3 shows the resulting median convergence profiles across runs of Algorithm 1 in terms of the FR error for the \mathbb{T}^2 example (left) and \mathbb{T}^4 example (right). For \mathbb{T}^2 , we observe the separable encoding achieves faster convergence speed. In contrast, the convergence behavior in the high-dimensional \mathbb{T}^4 case shows a more complex pattern: while separable encodings initially converge rapidly, their convergence rate slows considerably later in the training. The non-separable encodings are a bit slower to begin with, but ultimately exhibit superior convergence speed when considering the entirety of the training duration, making

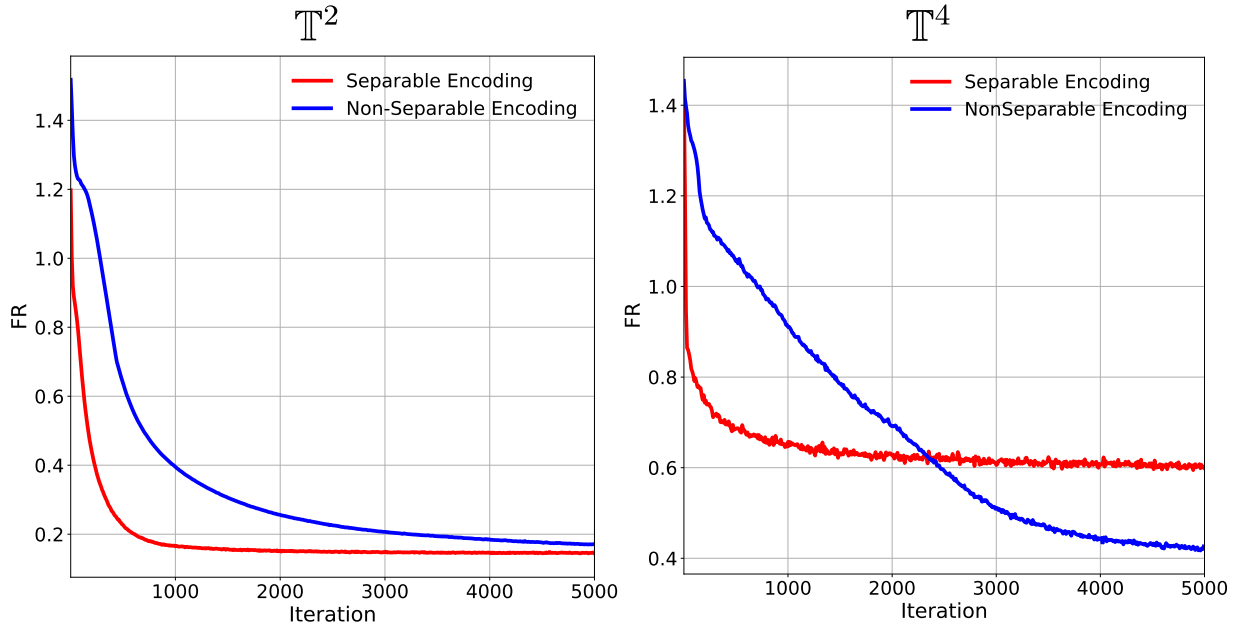


Figure S3: Median convergence profiles across runs of Algorithm 1 in terms of the FR error for the \mathbb{T}^2 example (left) and \mathbb{T}^4 example (right).

them more effective at controlling spectral bias in this regime.

As illustrated in Figure S2, the encodings appear to introduce different implicit biases. Specifically, the separable encodings concentrate all frequency oscillations along the same marginal axes, while the non-separable encodings distribute oscillations across multiple directions. Whether the implicit bias of the non-separable encodings consistently offer superior performance in high-dimensional domains remains an open question and an important avenue for future research.

Providing further context are the results of the “vanilla” ReLU MLP trained directly on spatial coordinates, presented in Table S1. This baseline approach effectively forms a low-frequency encoding (the identity encoding) that does not account for manifold structure, and exhibits significantly worse performance. These results further highlight the critical role of first-layer encodings $\boldsymbol{\eta}$ in the performance of the network architecture (5) estimated via Algorithm 1.

In practice, the ISE criterion in (13) can be used to select between encoding types. Table S2 reports the median ISE criterion at iteration $T = 5,000$, calculated using a small held-out test set. The results show a lower value for the separable encoding in the \mathbb{T}^2 case and a lower value for the non-separable encoding for the \mathbb{T}^4 case, consistent with the ground

	\mathbb{T}^2	\mathbb{T}^4
Separable Encoding	-6.876	-32.393
Non-Separable Encoding	-6.799	-38.473

Table S2: Median ISE criteria (Equation 13) at iteration $T = 5,000$ for different encoding types, calculated on a held-out test set.

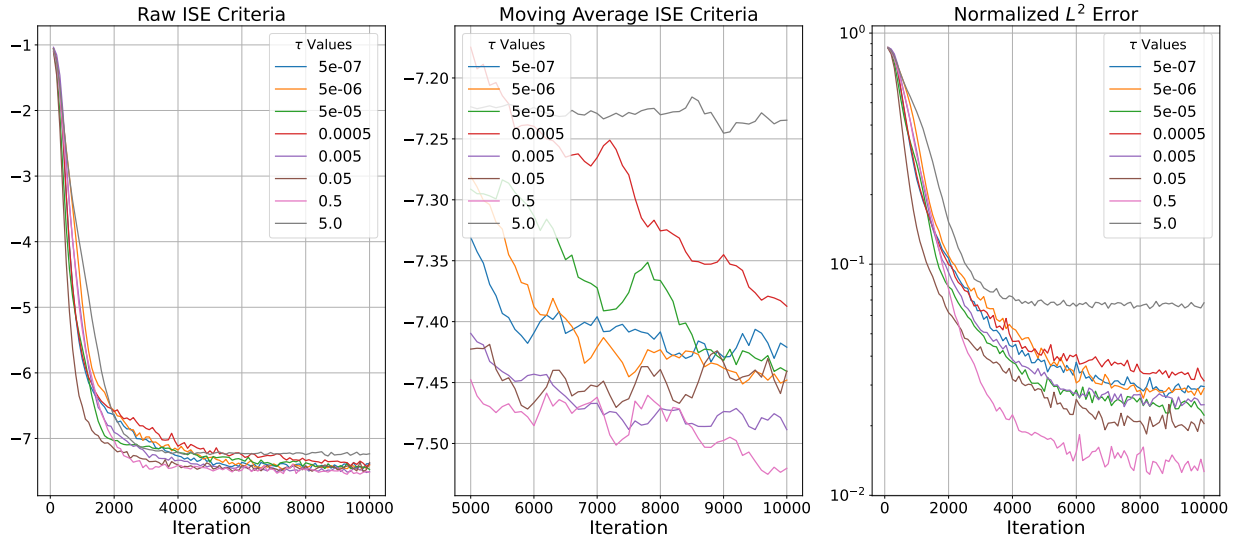


Figure S4: (Left) ISE criteria evaluated every 100 iterations of Algorithm 1 on the validation set. (Middle) Smoothed moving average of the ISE criteria over the final 5,000 iterations. (Right) Normalized L^2 error (nISE) sampled along the optimization trajectory.

truth performance observed in Figure S3. Since this criterion can be calculated without access to ground truth, it provides an effective method for selecting the η hyperparameter in practice.

S5.1.4 Effect of τ Parameter and Early Stopping

Figure S4 displays the optimization trajectory for a randomly selected replication of the \mathbb{T}^2 synthetic data experiments described in Section 5.1. The left plot shows the ISE criteria from Equation 13, evaluated on the validation set using density estimates obtained every 100 iterations of Algorithm 1. The middle plot shows a moving average of the same ISE criteria, calculated with a sliding window of 50 iterations to smooth out stochastic variations, over the final 5,000 iterations of the optimization trajectory. The right plot displays

the normalized ISE criteria (nISE) sampled at the same points along the optimization trajectory.

We observe a strong correspondence in the ordering of the τ curves with respect to the ISE criteria calculated on the validation set (left and middle plots) and the true normalized L^2 -error with the ground truth density function (right plot). Combined with the strong aggregate simulation results reported in Section 5.1, this indicates strong performance for our hyperparameter selection scheme.

The correspondence between these orderings also makes the moving averages of the ISE criteria a natural criterion for early stopping, i.e., dynamically terminating Algorithm 1 before reaching T when the value plateaus. While not strictly necessary for fitting quality, since our roughness-based regularizer effectively controls “over-fitting” behavior of the deep network estimator, such early stopping may offer significant benefits by accelerating total training time. Further exploration of early stopping within this context is left for future work.

S5.2 Neural Connectivity Data Analysis

Figure S5 shows the marginal density function estimates, \tilde{f}_E , for connections originating from the medial orbitofrontal cortex (MOFC) for three randomly selected ABCD subjects. Figure S6 maps these marginal density functions onto the cortical surface for biological interpretability. While similar overall structures are apparent in all subjects, there is significant between-subject variability in the high-resolution details.

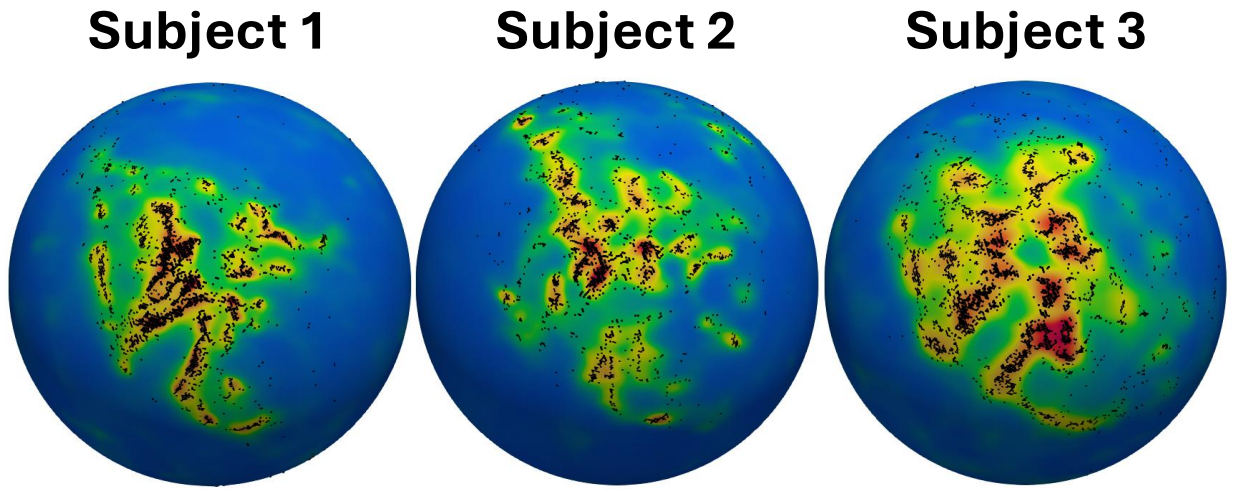


Figure S5: Marginal density function estimates for connections from the medial orbitofrontal cortex (MOFC), generated using our method (NeuroPMD) for three randomly selected ABCD subjects (left, middle and right). Black dots represent the endpoints connected to the MOFC. Color scales are normalized within each image to emphasize differences in the shape of the functions.

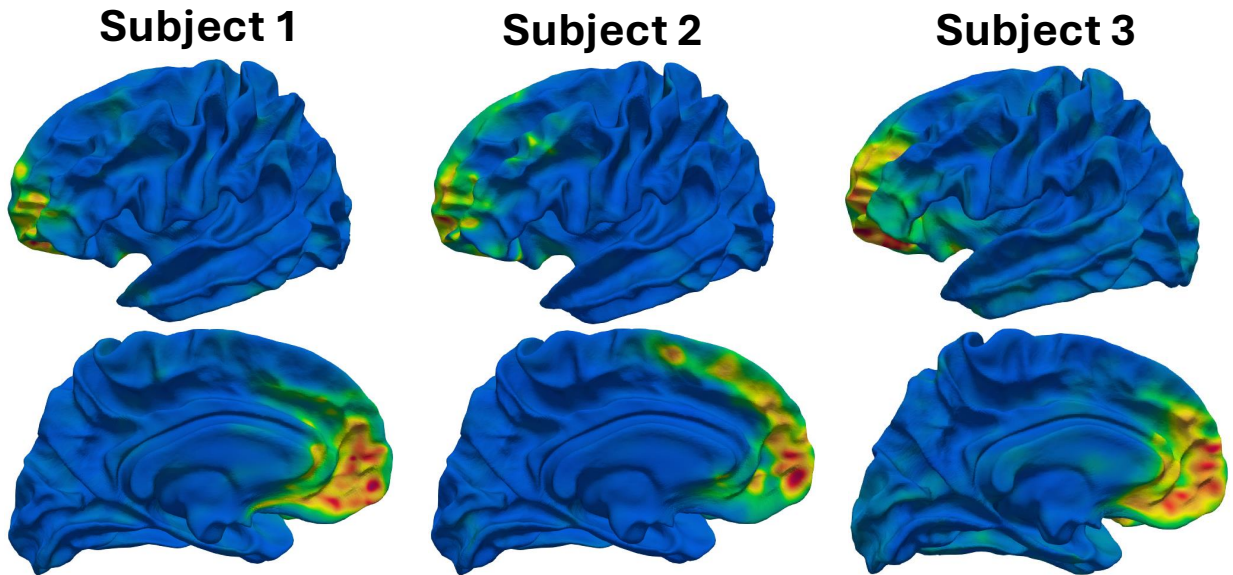


Figure S6: Same as Figure S5, with marginal density functions mapped to the cortical surface.

REFERENCES

Bottou, L., Curtis, F. E., and Nocedal, J. (2018). Optimization methods for large-scale machine learning. *SIAM Review*, 60(2):223–311.

- Boyd, S. and Vandenberghe, L. (2004). *Convex optimization*. Cambridge university press.
- Canzani, Y. (2013). *Analysis on manifolds via the laplacian*. Harvard University.
- Harlim, J., Jiang, S. W., and Peoples, J. W. (2023). Radial basis approximation of tensor fields on manifolds: From operator estimation to manifold learning. *Journal of Machine Learning Research*, 24(345):1–85.
- Mardia, K. and Jupp, P. (2009). *Directional Statistics*. Wiley Series in Probability and Statistics. Wiley.
- Osada, R., Funkhouser, T., Chazelle, B., and Dobkin, D. (2002). Shape distributions. *ACM Trans. Graph.*, 21(4):807–832.
- Rahaman, N., Baratin, A., Arpit, D., Draxler, F., Lin, M., Hamprecht, F., Bengio, Y., and Courville, A. (2019). On the spectral bias of neural networks. In Chaudhuri, K. and Salakhutdinov, R., editors, *Proceedings of the 36th International Conference on Machine Learning*, volume 97 of *Proceedings of Machine Learning Research*, pages 5301–5310. PMLR.
- Smith, L. N. (2017). Cyclical learning rates for training neural networks. In *2017 IEEE Winter Conference on Applications of Computer Vision (WACV)*, pages 464–472.
- Smith, L. N. and Topin, N. (2019). Super-convergence: very fast training of neural networks using large learning rates. In Pham, T., editor, *Artificial Intelligence and Machine Learning for Multi-Domain Operations Applications*, volume 11006, page 1100612. International Society for Optics and Photonics, SPIE.
- Zappa, E., Holmes-Cerfon, M., and Goodman, J. (2018). Monte carlo on manifolds: Sampling densities and integrating functions. *Communications on Pure and Applied Mathematics*, 71(12):2609–2647.